Evaluating Potential Impact of Seeding Tropical Cyclones with Aerosols in the Numerical Model ICON

Master's Thesis

Kenneth Chan

kechan@student.ethz.ch

21-950-936

Department of Earth Sciences, ETH Zürich

Institute for Atmospheric and Climate Science

Supervisors:

Nadja Omanovic[1], Institute for Atmospheric and Climate Science, ETH Zürich

Prof. Ulrike Lohmann, Institute for Atmospheric and Climate Science, ETH Zürich

20 March, 2023

[1]Main supervisor

Summary

Tropical cyclones (TCs) approaching land threaten populated regions and can lead to enormous socio-economic damage and casualties. Searching for solutions to reduce damage associated with TCs, the concept of TC geoengineering was explored in numerical models by seeding clouds at different locations within a TC in attempts to modify its structure. Successful structural modification of a simulated TC could inform real world strategies that ultimately minimize the hazards brought by TCs. Because the mechanisms in which cloud condensation nuclei (CCN) interact with TCs are manifold, further investigation is required to understand the microphysical processes that may ultimately modify the cyclone's structure. In this project, the regional ICON model was used to perform numerical simulations of TCs over the North Atlantic, using ECMWF ERA5 reanalysis as initial and boundary input data. Additional CCN were artificially injected into different locations away from the centre of the TC. Results show that the injected CCN were advected by the TC radial inflow towards the eyewall and invigorated convection there, causing further intensification of the TC. Cloud structure changed due to the change in buoyancy. There was little change in total precipitation in the TC, but the precipitation pattern changed, with enhanced precipitation in the eyewall and suppressed precipitation at larger radii. The way the TC responded to the additional CCN also depended on the overall structure and the intensification trend of the TC upon seeding.

Contents

Contents

1. Background

Tropical cyclones (TCs) are a major weather hazard in coastal regions. They pose a severe threat to millions of people's lives and properties every year (Geiger et al., 2018). With the enormous amount of moisture picked up from the tropical ocean and a very steep pressure gradient especially near its centre, TCs cause extensive damage by major flooding through storm surges and torrential rainfall (Woodruff et al., 2013; Farfán et al., 2014; Needham et al., 2015), and fierce winds (Harper, 1999). It is important from the societal aspect to quantify the destruction power of a TC to facilitate disaster preparedness upon the approach of a TC. In light of that, there are various proposed indices, attempting to quantify a TC's destructive potential. The destruction caused by TCs does not correspond linearly to its maximum wind speed. These destruction-indicating indices are often connected to a certain power of the TC wind speed (Table 1.1). This implies that the TC's destructive potential increases rapidly as its maximum wind becomes stronger (Willoughby et al., 1985). Hence, even a small reduction in maximum wind could effectively mitigate risks associated with TCs.

Table 1.1.: TC destruction-indicating indices related to powers of wind speed

Index	Power of wind speed	Author
Accumulated Cyclone Energy	2	Bell et al., 2000
Integrated Kinetic Energy	2	Powell and Reinhold, 2007
Power Dissipation Index	3	Emanuel, 2005
-	7 to 10	Nordhaus, 2006

Looking for a solution to reduce TC-related damage, numerous efforts have been put into understanding the thermodynamical and microphysical processes that take place in a TC and drive its development (Wang & Wu, 2004). Some of these efforts attempted to investigate the effect of an artificial intervention in TCs, with an aim of weakening them to alleviate losses. Yet, the understanding of the dynamics in TCs is limited, such that the concept of artificial TC modification is largely restricted to numerical simulations.

1.1. Structure and Circulation of TC

TCs are low pressure systems with a warm core that carry positive relative vorticity, i.e., cyclonic rotation in the lower troposphere. A typical mature TC consists of an eye embedded in a central dense overcast, characterised by deep convection, and the spiral rainbands of the TC extending radially outwards (Emanuel et al., 2003; Lohmann et al., 2016), (Figure 1.1).
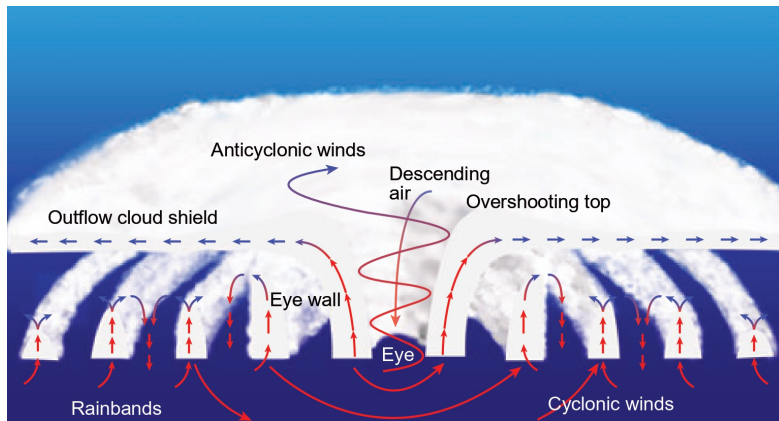

Figure 1.1.: Schematic of the three-dimensional structure of a TC. The solid red arrows at the surface show the cyclonic flow of the TC; the downward arrow in the eye indicates the subsidence and the upward circulating arrow indicates the change in rotation axis from the surface to the top. The short arrows in the rainbands denote the rising and sinking air and the short blue horizontal arrows denote the outflow at cloud top. Adapted from Figure 10.20 in Lohmann et al. (2016).

The airflow in a frictionless rotating system can be approximated by the gradient wind balance, in which the pressure gradient force (PGF) is balanced by the centrifugal force and the Coriolis force. Since TCs are low pressure systems, the PGF in a TC always points towards its centre. The centrifugal force points away from the TC centre. The Coriolis force points to the right to the direction of motion in the Northern Hemisphere. However, the presence of friction, predominantly near the surface and in the boundary layer, which acts to decelerate motion and points in its opposite direction, breaks down the gradient wind balance. Subgradient wind dominates in the outer region within the boundary layer such that the radial wind is directed towards the centre, while su-

pergradient wind occurs within the eyewall, in which the radial wind is directed away from the centre (Montgomery & Smith, 2014). An illustration of gradient wind balance, subgradient wind and supergradient wind in a TC is depicted in Figure 1.2.

a Gradient wind balance in a frictionless flow

b Subgradient wind in the outer region of a TC in the boundary layer

c Supergradient wind between the eyewall and the centre of a TC in the boundary layer
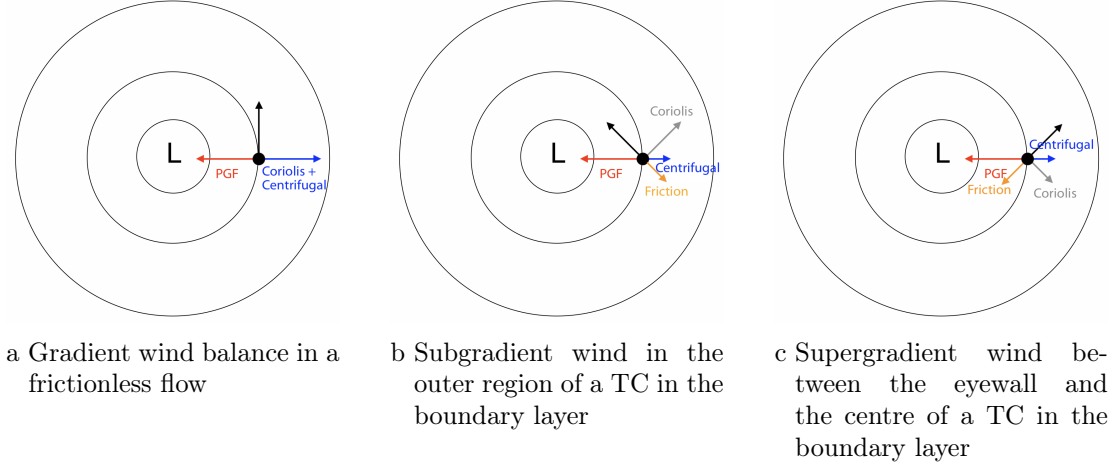
Figure 1.2.: The black arrow shows the direction of motion of the black dot in a TC in the Northern Hemisphere (centre marked with "L"). The pressure gradient force (PGF) points towards the TC centre, while the centrifugal force points away from the TC centre. The Coriolis force points to the right of the direction of motion. Friction is significant in the boundary layer and points opposite to the direction of motion. The lengths of the arrows are not drawn to scale.

The convergence of supergradient wind and subgradient wind under the eyewall leads to ascent there. This is called the primary circulation of the TC (Lohmann et al., 2016). This can be illustrated with the concept of absolute angular momentum $M = vr + \frac{1}{2}fr^2$, where r is the radius, f is the Coriolis parameter, which increases with latitude and v is the tangential wind speed (Holland, 1983). M is conserved in the absence of an external force acting on the system. However, the conservation of M does not hold in the boundary layer due to the presence of friction, which reduces M towards to the centre. Although M decreases towards the TC centre as friction acts to dissipate it, v nevertheless increases towards the centre due to decreasing r. This is known as the boundary layer spin-up mechanism (Montgomery & Smith, 2017). When v increases fast enough, such that the radial inflow is brought to small radii with little loss of M, i.e., the dissipation rate of M by friction does not keep up with the increasing wind, the wind

1. Background

becomes supergradient within the eyewall (Smith et al., 2009).

However, as an air parcel ascends in the eyewall in the primary circulation, it decelerates as the radius increases due to the conservation of M. This would slow down the TC's circulation above the boundary layer (Greenspan & Howard, 1963; Montgomery & Smith, 2017). Hence, a secondary circulation, which is driven by thermodynamics, is required to drive the TC's circulation above the boundary layer. This is achieved by the latent heat release in the eyewall, in which the energy is extracted from the warm ocean. Upon condensation in the eyewall, the latent heat release causes local heating of the air parcel. This leads to an increased buoyancy of the air parcel and causes it to lift, resulting in a local reduction in pressure. An additional inflow from below follows, while a strong outflow occurs at the tropopause (Montgomery & Smith, 2014). Figure 1.3 shows the azimuthally averaged radial inflow in a TC. Azimuthal average plots are commonly used in TC analyses, because the circulation of a TC is approximately axisymmetric. A strong inflow is found in the boundary layer, which is related to the primary circulation. The radial flow associated with the secondary circulation above the boundary layer is relatively weak (Montgomery & Smith, 2017).

Such circulation in an ideal and mature TC could be viewed as a heat engine in a Carnot cycle, in which the gas doing (positive) work experiences isothermal expansion and absorbs heat at a higher temperature, followed by adiabatic expansion (cooling). Afterwards, the gas isothermally compresses and releases heat at a lower temperature, followed by adiabatic compression (warming). During the adiabatic processes, there is by definition no heat exchange with the environment (Halliday et al., 2014). A schematic diagram of the Carnot cycle in a TC is shown in Figure 1.4. An air parcel experiences isothermal expansion at the inflow towards the centre in the boundary layer. Heat is gained through the acquisition of moisture through evaporation of sea water. The equivalent potential temperature (θ_e) is a useful quantity in analysing the structure and circulation of TCs. It is defined as the temperature of the air would have if all its moisture were condensed during a pseudo-adiabatic ascent and then brought down to a reference pressure ($1000\,\mathrm{hPa}$). The equation of θ_e is given by $\theta_e = T(\frac{p_0}{p_d})^{\frac{y_d R}{c_p}} \exp(\frac{l_v y_{vs}}{c_p T})$,
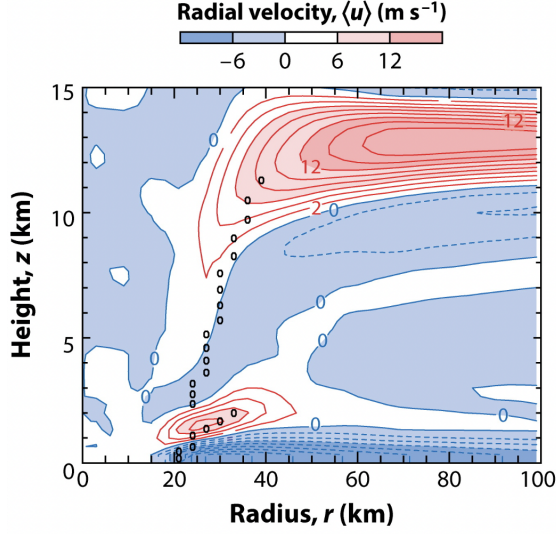
Figure 1.3.: Radius-height cross section of azimuthally averaged radial velocity in a TC. Contour intervals are in $2\,\mathrm{m\,s^{-1}}$. Positive values are in red and indicate radially outward flow. Negative values are in blue and indicate radially inward flow. Strong radial inflow is found below $1\,\mathrm{km}$ height. Black dotted circles show the location of the maximum tangential wind speed at each height. Taken from Figure 2a of Montgomery and Smith (2017).

where T is the absolute temperature, p_0 is the reference pressure, p_d is the dry air pressure, y_d and y_{vs} are the mole fractions of dry air and vapour respectively, R is the air constant, c_p is the air specific heat capacity at constant pressure and l_v is the latent heat of vapourisation (Lamb & Verlinde, 2011). θ_e increases during isothermal expansion, because of the increase in specific humidity from evaporation and the pressure decrease (A→B). The air parcel rises and expands adiabatically at the eyewall with constant θ_e, as there is no heat exchange and the latent heat released by condensation remains within the air parcel (B→C). θ_e decreases during isothermal compression at the tropopause due to clear sky radiative cooling, which is balanced by adiabatic compression (C→D). Finally, the air parcel returns to the boundary layer at the periphery of the TC by adiabatic compression with minor change in θ_e (D→A). The thermal efficiency in the Carnot cycle η, which refers to the efficiency with which the energy input is converted to work, is given by $\eta = 1 - \frac{T_C}{T_W}$, where T_C and T_W are the absolute temperatures of the cold reservoir

(tropopause) and the warm reservoir (sea surface), respectively (Halliday et al., 2014). The strongest wind speed of a TC is found under the eyewall, where the generation rate of available energy from latent heat and sensible heat flux is in equilibrium with the mechanical dissipation rate by the drag exerted by the waves.
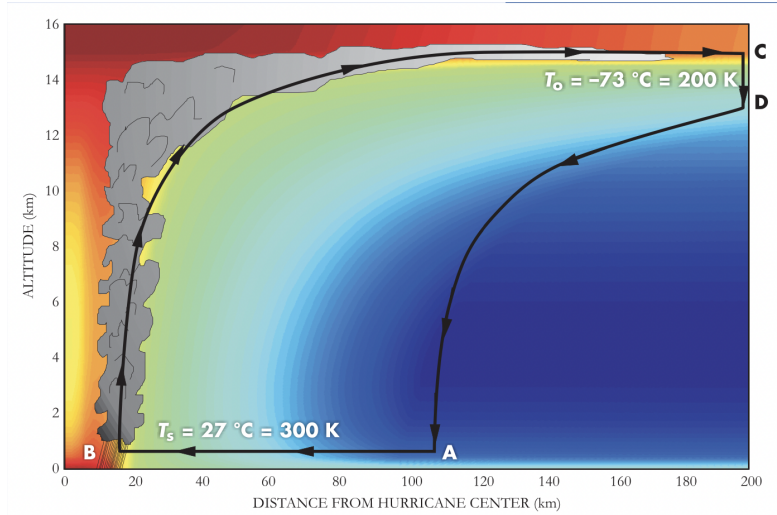

Figure 1.4.: Carnot cycle in a TC. An air parcel experiences isothermal expansion with a gain in θ_e in the boundary layer (A→B), ascends and adiabatically cools in the eyewall (B→C), isothermally compresses by radiative cooling and descent with a decrease in θ_e (C→D), and finally descends and adiabatically warms at the periphery of the TC (D→A). Colours show θ_e surfaces, with warmer colours indicating higher values. With the temperatures of the cold reservoir (outflow at the tropopause, T_O) and the warm reservoir (sea surface, T_S), one can compute the Carnot efficiency $\eta = 1 - \frac{200}{300} = \frac{1}{3}$. Adapted from Emanuel (2006).

1.2. Aerosols Acting as Cloud Condensation Nuclei and Ice Nucleating Particles in TC

Hoping to reduce casualties and damage brought by TCs, various schemes have been proposed to modify their structure, in particular to weaken the cyclones. The pioneering project attempting to artificially weaken TCs was the project STORMFURY between 1962 and 1983 (Willoughby et al., 1985). The STORMFURY project aimed at facilitating

cloud formation outside the eyewall, by using silver iodide as a cloud seeding agent to initiate ice formation of the supercooled water there. The goal was to invigorate convection further away from the eyewall, by letting the supercooled water freeze and release latent heat of fusion, such that the strongest updraft shifts outward and creates a larger eye. It was hypothesised that the wind speed in the TC would decrease if the eye enlarged due to a reduction in the horizontal pressure gradient and the conservation of angular momentum (Smith, 1981). The STORMFURY experiment was carried out in different TCs. Some positive results were achieved, where the wind speed of the seeded TCs was observed to decrease as the storm radius increased. Nevertheless, STORMFURY ended in 1983, as observations indicated that there was too little supercooled water in TCs to significantly impact the physics of TCs. Moreover, the concept of weakening the storm by enlarging its radius was discovered to resemble the eyewall replacement cycle, which naturally occurs in severe TCs. A "double eyewall" is often observed in strong TCs. As the TC strengthens, the wind speed further increases. Supergradient winds can occur further away from the primary eyewall, and a secondary eyewall forms outside of the primary eyewall. The secondary eyewall intercepts the inflow towards the primary eyewall, leading to the decay of the primary eyewall, which is known as the eyewall replacement cycle. As the secondary eyewall has a larger radius, the wind speed is typically reduced during the eyewall replacement cycle (Willoughby et al., 1982; Sitkowski et al., 2011; Zhou & Wang, 2011).

Despite the failure of STORMFURY to modify and weaken TCs, there has been ongoing researches seeking other methods to artificially modify TCs. It was recognised that the Saharan Air Layer (SAL), characterised by outbreaks of very dry Saharan air carrying dust blowing westward over the tropical Atlantic, often associated with a mid-level easterly jet (Carlson & Prospero, 1972; Dunion & Velden, 2004), influences the intensity of North Atlantic TCs. The mechanism with which the SAL influences TC intensity is manifold. The SAL can bring drier air and stronger vertical wind shear which inhibit TCs from intensifying (Wu, 2007). The radiative forcing from the dusty layer (Ma et al., 2012), as well as the intrusion of Saharan air of warm origin into the Atlantic atmosphere

(Dunion & Velden, 2004) can perturb the atmospheric stability.

There is also an aerosol indirect effect, which corresponds to the cloud microphysical effect brought by aerosol particles, and may also affect the development of TCs. This can shed light on a new potential way to artificially modify TCs by introducing aerosols acting as cloud condensation nuclei (CCN), instead of silver iodide acting as ice nucleating particles (INP) as in STORMFURY, into a TC. These Saharan dust particles, as well as aerosols originating from the ocean or from anthropogenic activities, can act as CCN, which play a crucial role in cloud microphysics.

Formation of warm clouds requires CCN. These CCN containing water-soluble substances help to initiate the liquid phase more effectively, because water particles attach themselves to the soluble matter and dissolve them. The solute ions help retain water in the condensed state by lowering the vapour pressure (Lamb & Verlinde, 2011).

Under a high concentration of CCN, a higher concentration of droplets will form as a result. The droplets compete for the available water vapour. Due to greater depletion of water vapour, the droplet size becomes smaller (Lamb & Verlinde, 2011). The collision and coalescence process, in which droplets collide and collect other droplets to form larger drops, is therefore suppressed. The droplets gain mass slower, such that they do not become sufficiently large rain drops and fall due to gravity, but remain smaller and are further lifted by the updrafts instead (Cotton et al., 2012), leading to a decrease in precipitation efficiency and a prolonged lifetime of the clouds (Lohmann & Feichter, 2005). Furthermore, these polluted clouds with smaller droplets scatter sunlight more effectively, which in turns leads to higher albedo of the clouds and has a cooling effect on climate, which is known as the Twomey effect (Lamb & Verlinde, 2011).

As these small droplets are lifted to supercooled levels by updrafts, the amount of supercooled water increases in the convective clouds. These supercooled cloud droplets can freeze and release extra latent heat. The cloud warms due to the extra latent heat and convection is further invigorated, leading to a stronger updraft at lower levels (Carrio & Cotton, 2011; Cotton et al., 2012; Rosenfeld et al., 2012).

1.3. Selected TC Modification Studies

1.3.1. Change in TC Intensity

Aerosols from the SAL or anthropogenic activities typically intrude the TC from the peripheral rainbands. Researches have been investigating the impacts of these aerosols on TCs upon intrusion into rainbands. Rosenfeld et al. (2007) simulated the injection of aerosols in the rainbands of Hurricane Katrina in 2005 using the WRF model (Michalakes et al., 2001; Michalakes et al., 2005; Skamarock et al., 2005) with a double nested grid with resolutions of 9 km and 3 km. Anticipating that an increased CCN concentration should impede collision and coalescence, they performed the simulation by disallowing collision of the droplets. It was found that the mass flux into the eyewall was decreased as it was intercepted by the invigorated convection in the rainbands. Convection near the centre weakened and caused a reduction in radial wind speed. However, a cold pool formed by downdraft initiated from the precipitation, because some precipitation evaporated and consumed latent heat. The cold pool later suppressed convection and forced the inflow to rise closer to the centre, which eventually led to a more compact eye and increased wind speed. Zhang et al. (2007) simulated aerosol indirect effect more realistically by introducing aerosols in the RAMS model (Cotton et al., 2003) instead of switching off the collision process. They forced a consistent layer of SAL dust between 1 km and 5 km and simulated its effect on the development of an idealised pre-TC vortex, with three nested domains with horizontal resolutions of 24 km, 4 km and 2 km, and with a two-moment microphysics scheme. They found that the number of activated CCN was larger when a simulated SAL was present. Furthermore, the TC in a SAL with high CCN concentration was characterised by a weaker intensity and a larger eye. It was observed that the diabatic heating due to latent heat release was not concentrated in the eyewall, but was found in the outer rainbands. Khain et al. (2008) combined a high-resolution 2D mixed-phase cloud model with spectral bin microphysics (Khain & Sednev, 1996; Khain et al., 2004; Khain et al., 2005) with the WRF model, where the former can describe microphysical processes in more detail and evaluate the aerosol effects on the vertical

profiles of liquid water and ice particles contents in individual clouds, when simulating a landfalling TC in the Gulf of Mexico intercepting continental aerosols. They showed that these continental aerosols invigorated convection $250\,\text{km}$ to $300\,\text{km}$ from the centre, and depleted the mass flux to the centre which caused the TC to weaken. They also found that intense and persistent peripheral lightning was a permanent feature of land-approaching TCs, because the ingested continental aerosols led to an increased amount of ice hydrometeors, which experienced more frequent collision and charge separation. Similar results showing TCs being weakened by a layer of a higher concentration of aerosols were also reported for the North Indian Ocean basin (Hazra et al., 2013). Zhang et al. (2009) simulated the development of an idealised mature TC with varied CCN concentrations being injected at the periphery. They used a similar simulation model setup as in Zhang et al. (2007), but the injection of aerosols was only employed at the TC periphery but not near the eyewall. They suggested that the downdraft and evaporative cooling at the spiral rainbands blocked air with high θ_e from flowing into the eyewall, which resembled the effects of a secondary eyewall on a primary eyewall. Enhanced convection in the rainbands led to a weakening of the eyewall, as the high θ_e, i.e., warmer and moister inflow was replaced by low θ_e, i.e., cooler and drier inflow from downdrafts in the rainbands. This resulted in a lower wind speed and higher central pressure of the TC (Rosenfeld et al., 2007; Carrio & Cotton, 2011; Rosenfeld et al., 2011; Cotton et al., 2012; Rosenfeld et al., 2012). A schematic diagram illustrating the weakening of TC by peripheral aerosol intrusion is shown in Figure 1.5.

Nevertheless, there are other studies suggesting that aerosols may facilitate TC intensification through the aerosol indirect effect. Cotton et al. (2012) particularly pointed out that the life cycle of a TC, that ingested aerosols, was characterised by an initial intensification followed by an extended period of weakening. This was because the convection of the TC during its pre-mature stage was relatively weak and there were no distinct peripheral spiral rainbands, such that the aerosols were able to penetrate to the eyewall and invigorate convection there. When the TC developed to maturity, the weakening occurred through the mechanism illustrated previously. Liang et al. (2021) used
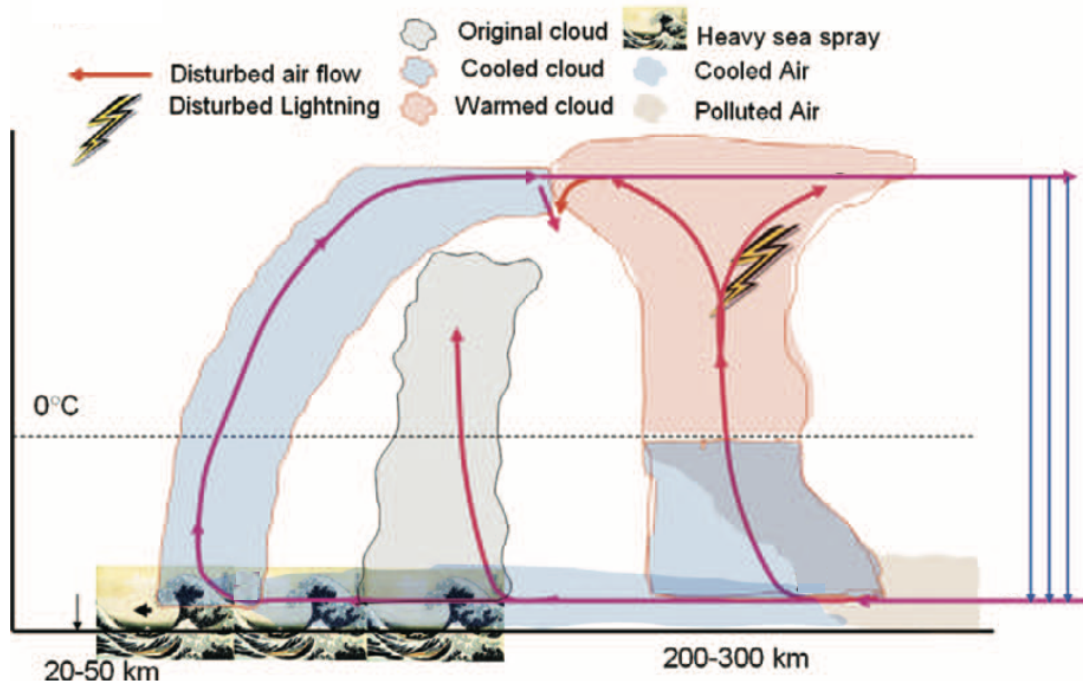
Figure 1.5.: Conceptual model of TC structure disturbed by aerosols at peripheral rain-
bands. Pollution of aerosols inhibits warm rain formation by decreasing
droplet size in peripheral clouds. Droplets are carried to supercooled levels,
where they freeze and release extra latent heat. Clouds are also electrified
due to a more frequent collision of hydrometeors. Convection is invigorated
at the peripheral rainbands, reducing the warm and moist inflow into the
eyewall. Evaporative cooling due to precipitation cools the low-level air at
the peripheral rainbands. The cool air flows into the eyewall and causes the
weakening of the eyewall. The circulation closes far away from the centre
by the descending, adiabatically compressing air (blue line). Adapted from
Figure 8b in Rosenfeld et al. (2012).

the WRF model with a chemistry-aware module (Grell et al., 2005), and a two-moment
microphysics scheme to simulate a TC approaching the Asian continent, from which an-
thropogenic aerosols intruded the TC. They suggested that the aerosols penetrated into
both the peripheral rainbands and the eyewall. Warm rain formation would be sup-
pressed in both regions, but the difference was that the updraft in the eyewall was much
stronger than that in the peripheral rainbands, which led to more frequent collisions of
supercooled water droplets with ice-phase particles in the freezing levels, and more latent

heat released by freezing, resulting in the TC intensification. Herbener et al. (2014) further offered another explanation on the aerosol-stimulated intensification. They used the RAMS model featuring a bin-emulating bulk microphysical scheme that includes three liquid and five ice hydrometeor species. The results of their simulations suggested that the radial inflow of a TC caused the aerosols to penetrate through the outer region of the TC and reach the eyewall. The increased concentration of CCN suppressed warm rain formation in the eyewall, favouring cloud droplets to rise to supercooled levels through the updraft and release more latent heat there. This led to an invigorated convection as well as a stretched vortex. Because of the stretching effect by the conservation of potential vorticity (Holton & Hakim, 2013), the vortex spun up and the wind speed increased. Due to continuity, environmental air with lower θ_e was drawn into the storm. The column of air in the outer region of the TC was cooled, which increased the low-level pressure in the outer region. This caused an increased horizontal pressure gradient but also a decreased storm size. Despite an increase in maximum wind speed, the authors suggested that the damage brought by the TC should be reduced because of the shrinking size of the cyclone. However, there has been so far no clear indication stating the conditions by which the aerosols are able to penetrate through the outer clouds into the eyewall instead of invigorating convection in the outer rainbands. The authors also noted the non-monotonic response of TC intensity to aerosol concentration in the simulations from Zhang et al. (2009) and provided a final remark, suggesting that the invigoration of convection by aerosols could take place both in the eyewall and in the outer rainbands simultaneously, which would offset each other. They hypothesised that when more aerosols intruded the TC, there would also be more aerosol particles being able to penetrate to the eyewall to invigorate convection, thereby offsetting the weakening effect. The simulation results of Jiang et al. (2016), who used the WRF model with the chemistry module, featuring a two-moment bulk scheme involving five types of hydrometeor species, also demonstrated the offsetting effect. They concluded that the TC intensity was insensitive to the concentration of aerosols. Braun (2010) also stated it was unclear whether the microphysical effects due to dust should strengthen or weaken a

TC. Cotton et al. (2007) noted that the results of cloud seeding simulations in TCs were highly sensitive to model configurations, and therefore suggested different simulations to be performed using independent model groups, as well as cases and initial conditions.

1.3.2. Change in TC Precipitation

Precipitation patterns in TCs may also change as a result of intrusion of aerosols. Zhao et al. (2018) studied TCs in the western North Pacific being intruded by East Asian anthropogenic aerosols using satellite observations. They analysed the correlation between atmospheric optical depth from MODIS (Levy et al., 2013) retrievals, which indicates aerosol concentration, and the rainfall amount and radius of TCs, determined from satellite rainfall retrievals (Huffman et al., 2010; Y. Lin et al., 2015). They noted the possibility of more severe coastal flooding upon landfall of aerosol-intruded TCs, as aerosols invigorated convection in the outer rainbands, eventually enhancing the total rainfall amount and area. Jiang et al. (2016) found that the precipitation rate of a TC was suppressed in extremely polluted cases, relative to the case with normal aerosol emission intensity. The autoconversion of cloud water, i.e., the growth of cloud droplets to rain drops by collision and coalescence, was suppressed because of the smaller droplet size. Ghosh et al. (2016) suggested a scheme to alleviate coastal flooding and the associated damage brought by TCs by artificially introducing giant CCN into the eyewall at $200\,\mathrm{m}$ above mean sea level prior to landfall, because larger CCN produced larger droplets and favoured warm rain processes such as collision and coalescence. Hence rainfall was enhanced prior to landfall, which lowered the risk of coastal flooding.

1.3.3. Change in TC Track

Effects on the track of TCs by artificial modification remain a major concern. Some simulations have shown that aerosol intrusion did not change TC trajectories significantly (W. Lin et al., 2011; Cotton et al., 2012; Jiang et al., 2016; Liang et al., 2021). In October 1947, a TC devastated Georgia and South Carolina in the United States. The storm sparked significant public interest not only because of the extensive damage brought by

the TC, but also because the TC was seeded with dry ice and made a dramatic turn on its track and hit the coast. Public outrage was sparked and the seeding was blamed upon, despite later studies discovering the peculiar track change was in fact related to an upper-level ridge that dominates the steering flow instead of the seeding (Willoughby et al., 1985; Norcross, 2007; NOAA Hurricane Research Division, 2017). After all, the possible influence on TC track through artificial modification remains one of the biggest ethical issues to investigate in artificial modification of TCs.

1.4. Aim and Structure of the Thesis

There remains many uncertainties regarding the overall effect of aerosols on the development and characteristics of TCs. Various mechanisms which alter the microphysics in TC clouds have been hypothesised, some of which could counteract each other and mask their effects. One of the biggest questions remains in whether or how the intrusion of aerosols in a TC invigorates convection at its periphery and in the eyewall. Different model configurations and choices of microphysical schemes may have also affected the modelling outputs. Therefore, this project aims at providing a different overview on the effects of aerosols on TCs. We seek to understand the mechanisms in which CCN at the peripheral rainbands impact the development of TCs. Section 2 describes the objectives of this project in detail. Section 3 outlines the data and methods used in this project. Section 4 discusses the results of the study. Section 5 describes the limitations of the study and provides a conclusion and final remarks to the project.

2. Objectives

In this project, numerical simulations on TCs with elevated CCN concentrations in the rainbands of a TC were performed. Simulations were conducted in the form of case studies, using the icosahedral non-hydrostatic (ICON) modelling framework (Zängl et al., 2015). In particular, this thesis project addresses the following research questions:

- How does injection of additional CCN in targeted regions in TCs influence the development and intensity of TCs?

- What is the impact of the injection of additional CCN in targeted regions in TCs on the precipitation tendency and cloud structure of TCs?

- Does, and if so how, the injection of additional CCN in targeted regions in TCs change their track?

3. Data & Methods

3.1. Data & Domain

Numerical simulations were performed with the ICON model version 2.6.4 in the limited area mode (Zängl et al., 2015). The data domain is from 0°N to 70°N, 120°W to 15°W and covers the North Atlantic basin. It has 50 vertical levels, topping at about 23 km, with increasing distances between levels with increasing altitude. The corresponding geometric heights of all model levels are listed in Table A.2.1. The R03B07 horizontal grid is used, which corresponds to a horizontal resolution of 0.125° (13 km). ECMWF ERA5 reanalysis data (Hersbach et al., 2020) were used to specify the initial and boundary conditions. 6-hourly data of zonal, meridional and vertical wind, temperature, surface pressure, surface geopotential, specific humidity, cloud water, cloud ice, rain, and snow were prescribed at the boundaries and were interpolated to individual

time steps. The model time step is $100\,\mathrm{s}$. Sea surface temperature and sea ice content were prescribed as monthly mean data. A two-moment parametrisation scheme by Seifert and Beheng (2006) for the cloud microphysics was adapted, including the prognostic CCN and INP modes. The ecRad radiation scheme (Hogan & Bozzo, 2016, 2018) was employed. The simulation results have an output frequency as 6-hourly data. TCs in the North Atlantic basin are the focus of this project.

3.2. TC Tracking Algorithm

The tracking algorithm is based on Kleppek et al. (2008) and Enz et al. (2023, in press). It uses mean sea level pressure, the vertical component of relative vorticity and temperature on the $300\,\mathrm{hPa}$ isobaric surface as criteria to identify the centre of TCs. Recalling TCs being warm-core low pressure systems with a cyclonic flow in the lower troposphere, the algorithm identifies grid points that satisfy the following requirements to be potential TC centres:

- The grid point has a local minimum of sea level pressure within a threshold radial distance r_p;

- To identify the TC's low-level cyclonic flow, the vertical component of relative vorticity at that grid point needs to exceed a threshold value ζ_{min} within the lower troposphere;

- To identify the TC's warm core, the temperature at the $300\,\mathrm{hPa}$ isobaric surface of the grid point has to be warmer by a threshold value ΔT_{core} than the mean temperature of the $300\,\mathrm{hPa}$ isobaric surface within a threshold radial distance r_T.

Multiple threshold values instead of a single threshold are adopted. All threshold combinations are used in parallel, resulting in varied flexibility in identifying storm centres. Multiple sets of identified potential TC centres will be generated. Weaker storms may be identified only with weaker constraints but not with stronger constraints. Stronger storms may satisfy both weaker and stronger constraints. To avoid false positives of

storm identification, the storm locations are retained only when more than a given percentage of the constraint combinations identifies the storm centre. Following the work of Enz et al. (2023, in press), the percentage of combinations required to confirm and retain the storm centre for storms of tropical depression, tropical storm and hurricane strength is chosen to be 10 %, 20 % and 50 % respectively. The threshold values are tabulated in Table 3.1.

Table 3.1.: Threshold values to identify potential TC centres

Variable		Threshold values				
r_p	[km]	50	100	150		
ζ_{min}	[s^{-1}]	10^{-6}	10^{-5}			
ΔT_{core}	[K]	0.5	0.75	1	1.25	1.5
r_T	[km]	50	100	200	300	400

TCs are assumed not to move faster than $20\,\mathrm{m\,s^{-1}}$. If the potential storm centres between two consecutive time steps are separated by a distance less than that stipulated by the above moving speed assumption, they are identified as the same storm and their locations are joined to form tracks.

3.3. CCN Injections

The control, unperturbed simulation is defined with a maritime background CCN concentration according to Segal and Khain (2006). The CCN concentration between the surface and $4000\,\mathrm{m}$ is $100\,\mathrm{cm^{-3}}$. Above this height, the concentration of CCN decays exponentially with a scale height of $2000\,\mathrm{m}$, i.e., the concentration of CCN drops by a factor of $\frac{1}{e}$ every $2000\,\mathrm{m}$. The minimum CCN concentration is $35\,\mathrm{cm^{-3}}$. The width of the CCN size distribution (σ_S) is 0.4. The geometric mean radius of CCN in the intermediate size mode is $0.03\,\mathrm{\mu m}$. In the perturbation simulations, CCN with a concentration of $1000\,\mathrm{cm^{-3}}$ were prescribed. The exact region to be seeded with CCN was determined manually according to the TC structure in the model. CCN were injected when the maximum wind speed of the storm first exceeded $33\,\mathrm{m\,s^{-1}}$, i.e., the threshold of a category 1 hurricane. The maximum wind speed was searched between the surface

17

and 3000 m height of the TC. CCN were replenished every model time step, i.e., every 100 s, for one hour.

4. Results & Discussion

4.1. The Target TCs

Two TCs were targeted for artificial CCN seeding. They both occurred in the 2005 Atlantic season. The cyclogenesis of the first TC (TC1 hereafter) was first detected on 28 Aug at 12 UTC over the North Atlantic Ocean. TC1 moved west to northwestwards and finally made landfall on 3 Sep at the coast near the border between Georgia and South Carolina of the United States. It weakened afterwards and dissipated on 5 September. The peak intensity of TC1 was reached on 3 Sep right before its landfall, with a maximum wind speed of $56\,\mathrm{m\,s^{-1}}$, equivalent to a category 3 hurricane. The second TC (TC2 hereafter) formed east-southeast of TC1 on 2 Sep. It took a recurving track and reached a maximum wind speed of $48\,\mathrm{m\,s^{-1}}$, equivalent to a category 2 hurricane. As TC2 moved poleward, it underwent extratropical transition. The TC warm core was finally lost on 9 Sep. The tracks of the two TCs in the control simulation (CTRL) are shown in Figure 4.1.

4.1.1. CCN Injection Setup

The category 1 threshold was reached on 30 Aug at 18 UTC for TC1 and on 4 Sep at 06 UTC for TC2. Seeding of aerosols in the perturbation simulations of each TC was therefore applied at the respective time step ($\mathrm{T_{seed}}$).

The cloud cover of the two TCs at $\mathrm{T_{seed}}$ is shown in Figure 4.2. TC1 was sheared despite attaining intensity of category 1, in which convection was more vigorous at the eastern flank of TC1, whilst it lacked convection at the western flank. As compared to TC1, TC2 already attained a rather clear eye structure when it reached the category 1 threshold, with a strong, prominent rainband in the south.
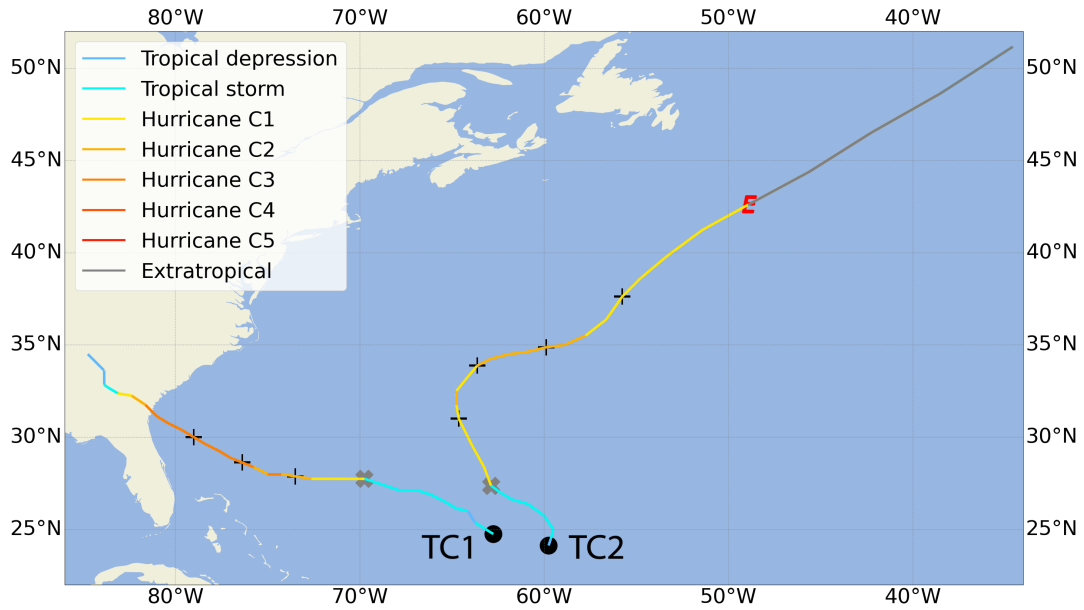
Figure 4.1.: Tracks of TC1 and TC2. Colours correspond to the maximum wind speed in the Saffir-Simpson Hurricane Wind Scale. The black dot indicates the location of cyclogenesis. The grey cross indicates the location where the category 1 threshold was reached and seeding was accordingly applied. The letter "E" marks the location where TC2 lost the warm-core feature of a TC and changed into an extratropical cyclone. Black plus signs indicate the 24-hourly positions of the TC after seeding and before landfall (TC1) or extratropical transition (TC2).
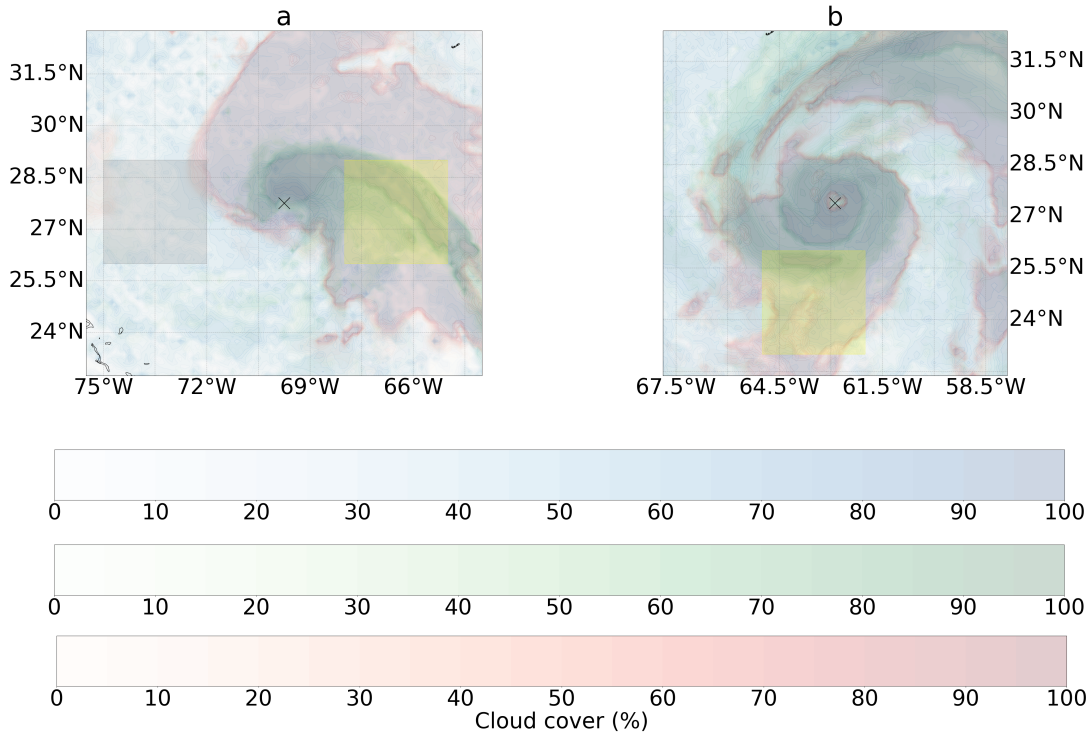
Figure 4.2.: Cloud cover at T_{seed} for (a) TC1 (30 Aug 2005 at 18 UTC) and (b) TC2 (4 Sep 2005 at 06 UTC). Low, mid and high level cloud cover are shown in blue, green, and red respectively. The black cross denotes the centre of the TC. TC1 was sheared, in which there was a prominent spiral rainband at the eastern flank, while the western flank was in lack of organised convection. TC2 had an eye which was better defined, and a strong, prominent rainband existed at its southern flank. The yellow boxes show the seeding area targeting the rainbands in the respective TCs to invigorate convection there. The grey box on the west of TC1 shows the area of the mirror experiment, in which additional CCN were injected where there was little preexisting convection, resembling TCs moving into a region with a high CCN concentration.

4. Results & Discussion

CCN were injected at one model level for each perturbation simulation. As shown in Figure 4.3, the lowest clouds in both TCs were at about model level 45, which corresponds to a geometric height of about 300 m. The seeding of the first perturbation simulation was restricted to one model level lower, i.e., to model level 46, which corresponds to a geometric height of about 220 m, anticipating the highest efficiency for cloud formation and invigoration of convection there. A $3° \times 3°$ square box, spanning 68°W to 65°W, 26°N to 29°N, overlapping the rainband at the eastern flank was seeded. This simulation was chosen as the "reference" seeding simulation (L46E hereafter). The choice of this seeding box is based on the mechanism shown in Figure 1.5 to weaken the TC, as well as that illustrated by previous researches (e.g., Zhang et al. (2009), Carrio and Cotton (2011), and Rosenfeld et al. (2012)). Another square box with the same size, spanning 75°W to 72°W, 26°N to 29°N, corresponding to the western flank of the TC which lacked convection, was seeded also at level 46 in another simulation (L46W hereafter). This resembles the effect of a westward-moving TC intersecting a region with high concentration of CCN, which can be of continental sources and therefore a naturally occurring effect. This effect was also simulated in other studies (e.g., Khain et al. (2010) and Liang et al. (2021)).

Recognising that the difference in the overall TC structure might impact the behaviour of CCN, a seeding box of the same size as that of TC1 was defined for TC2, spanning 65°W to 62°W, 23°N to 26°N, targeting this strong rainband at the southern flank. The seeding level was set at Level 46 (220 m) (L46S hereafter), the same level as the reference seeding simulation of TC1 (L46E).

As the seeding box lies within the boundary layer, it is mainly under the influence of the inflow of the TC. Subgradient winds in the outer region may advect the CCN towards the TC centre. One may expect this could mask an anticipated signal of TC weakening by invigorated rainband convection through the mechanisms postulated in Section 1. Further simulations were performed at higher model levels, namely model level 35 (1620 m) and level 29 (2880 m) for the seeding box on the east (L35E and L29E respectively hereafter).
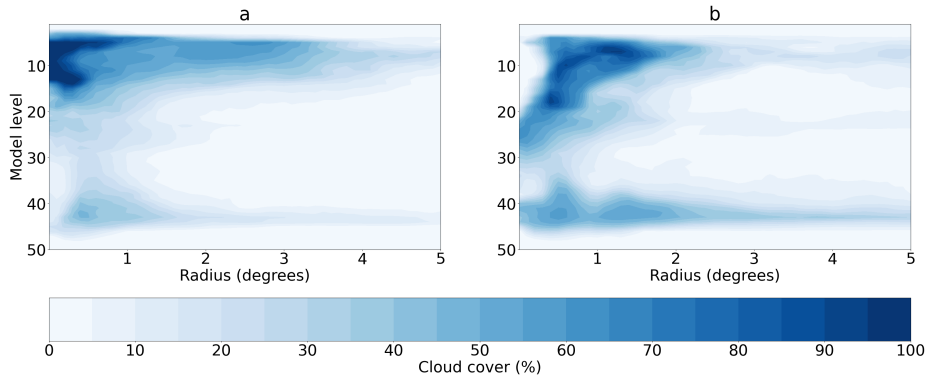
Figure 4.3.: Azimuthal average of cloud cover at T_{seed}, for (a) TC1 (30 Aug 2005 at 18 UTC) and (b) TC2 (4 Sep 2005 at 06 UTC)

Eventually, we have three groups of seeding simulations highlighting the effects of different factors, which are summarised in Table 4.1.

Table 4.1.: Simulation groups

Simulation Group	Focus	Simulations
Rainband	Effects of pre-existing rainbands	TC1: CTRL, L46E & L46W
Seeding height	Effects of seeding height and inflow of the TC	TC1: CTRL, L46E, L35E & L29E
TC structure	Effects of overall TC structure	TC1: CTRL & L46E; TC2: CTRL & L46S

4.2. Integrated Quantities & Time Series

4.2.1. TC Tracks

The tracks of TC1 and TC2 in the control simulation and perturbation simulations are shown in Figures 4.4 and 4.5 respectively. The perturbed tracks of TC1 attained a less northerly component as TC1 changed its course from moving west to northwest, and the landfall locations were slightly displaced to the south. However, the difference in tracks was small overall. The track difference between the control and perturbation simulations in TC2 was also small. The seeding of additional CCN caused no change in the timing of extratropical transition for TC2.
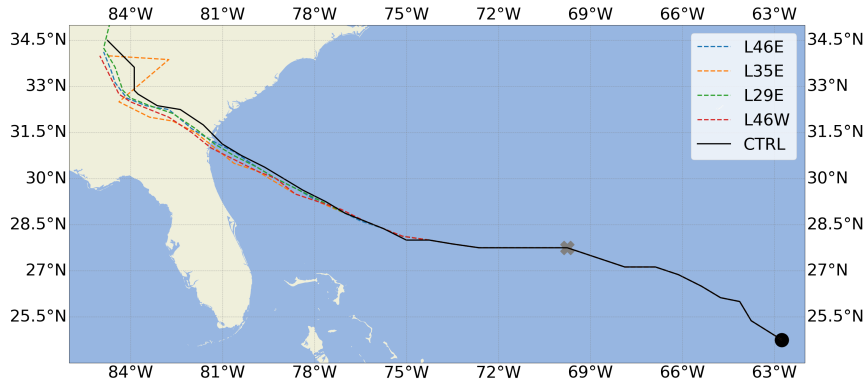
Figure 4.4.: Tracks of TC1 in the control simulation and perturbation simulations. The black dot indicates the location of cyclogenesis. The grey cross indicates the location where the category 1 threshold was reached and seeding was accordingly applied.
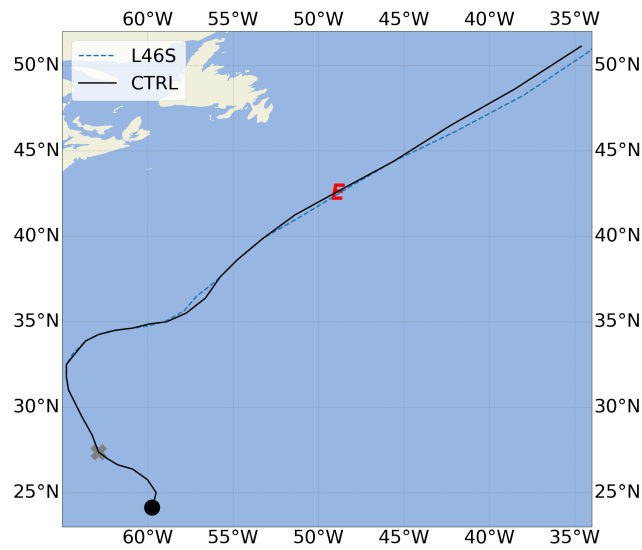

Figure 4.5.: Tracks of TC2 in the control simulation and perturbation simulation. The black dot indicates the location of cyclogenesis. The grey cross indicates the location where the category 1 threshold was reached and seeding was accordingly applied. The letter "E" marks the location where TC2 lost the warm-core feature of a TC and changed into an extratropical cyclone.

4.2.2. TC Intensities

The evolution of the simulated TC intensities as indicated by the minimum surface pressure and maximum wind speed, are shown in Figure 4.6. Their average intensities between the first time step after seeding and landfall (TC1) or extratropical transition (TC2) are shown in Table 4.2.

Table 4.2.: Average maximum wind speed and surface pressure of the simulated TCs in different simulations between the first time step after seeding and the time step of landfall (TC1) or extratropical transition (TC2).

Simulation	Maximum wind speed ($\mathrm{m\,s^{-1}}$)	Surface pressure (hPa)
CTRL (TC1)	50.41	961.38
L46E	54.86	959.19
L46W	53.39	959.13
L35E	53.83	959.02
L29E	54.17	959.19
CTRL (TC2)	41.64	972.57
L46S	42.81	970.85
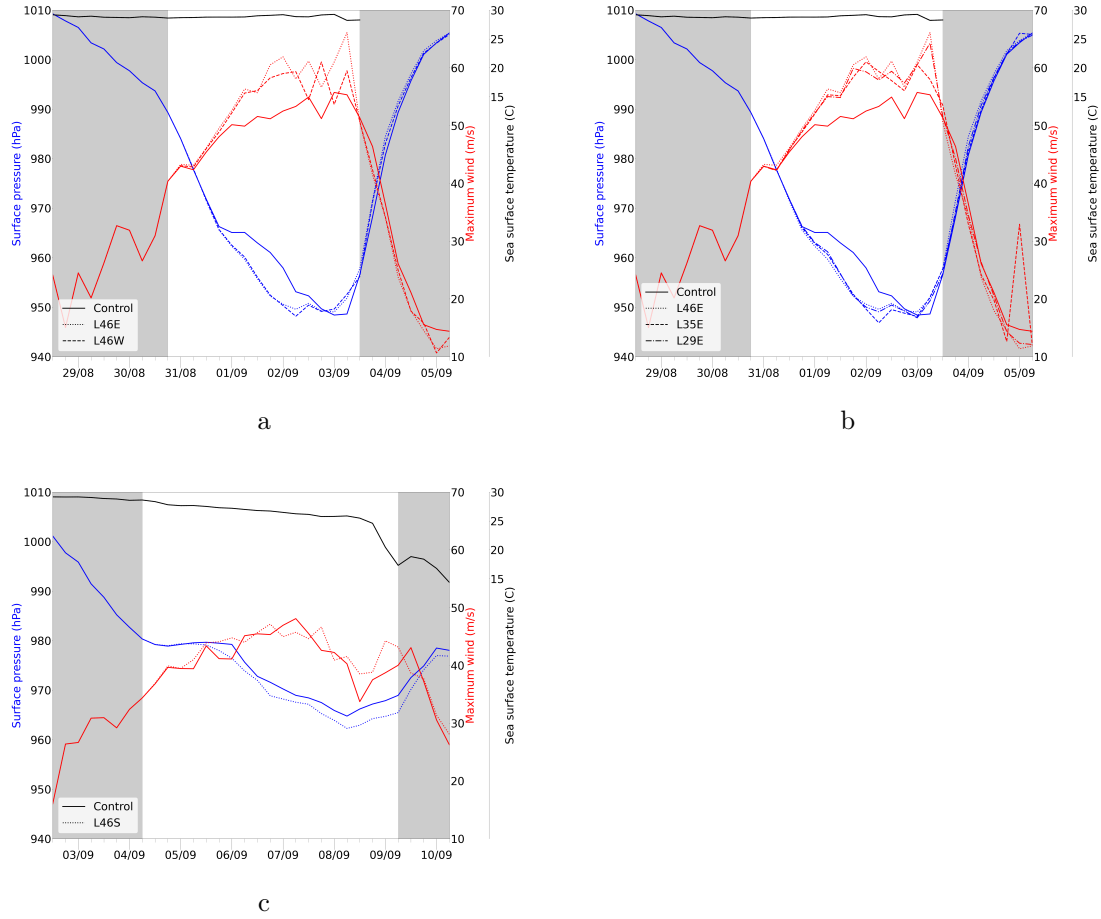
Figure 4.6.: Intensity evolution for (a) the rainband group simulations (TC1), (b) the seeding height group simulations (TC1) and (c) TC2 simulations. The blue lines and red lines show the minimum surface pressure and the maximum wind speed of the TC respectively. The black line shows the sea surface temperature at the centre of the TC. In the perturbation simulations of TC1, there was a rapid intensification episode on 1 Sep. The maximum wind speed was also higher than the control simulation. The intensity difference for TC2 was relatively minor, with a slight decrease in surface pressure upon seeding. The shaded time steps correspond to the time before seeding and after landfall (TC1) or extratropical transition (TC2) and are not the focus of this study.

4. Results & Discussion

TC1

As shown in Figures 4.6a and 4.6b, the perturbed TCs, regardless of location and height of CCN seeding, deepened more rapidly than the control simulation upon injection of extra CCN. The (first) surface pressure minimum was attained one day before that of the control TC. The control TC attained its surface pressure minimum right before its landfall on 3 Sep, while the perturbed TCs intensified faster. The surface pressure decreased rapidly on 1 Sep and reached the surface pressure minimum on 2 Sep and maintained it until landfall. The average surface pressure of the perturbed TCs between seeding and landfall was about 2 hPa lower than that of the control TC.

In terms of maximum wind speed, the perturbed TCs attained a higher maximum wind speed than the control TC. Following the rapidly decreasing surface pressure on 1 Sep, the maximum wind speed of the perturbed TCs also increased more rapidly than the control TC on 1 Sep. They further intensified between 2 and 3 Sep before making landfall despite the surface pressure did not decrease further, resulting in a higher maximum wind speed in their respective life cycle than the control TC. They attained the maximum intensity equivalent to a category 4 hurricane right before landfall, which was stronger than the control TC which only reached category 3. There was no significant difference in the rate of intensity change after landfall, after which the TC weakened and dissipated.

TC2

As shown in Figure 4.6c, TC2 in the perturbation simulation experienced a more significant pressure drop than in the control simulation upon seeding. The perturbed TC attained a minimum surface pressure about 5 hPa lower than the unperturbed TC.

The difference in maximum wind speed between the control and perturbed TCs was minimal, despite the perturbed TC attaining a vortex with lower surface pressure throughout the simulation period. They continued their intensification trend until 8 Sep, when the sea surface temperature dropped below 25 °C which was unfavourable for further TC development. Both TCs slightly reintensified upon extratropical transition but continued their decline afterwards.

4.2.3. TC Precipitation

The average 6-hourly precipitation of the TCs is shown in Table 4.3. There was no significant change in total precipitation in both TCs upon seeding. The difference in total precipitation in individual perturbation simulations of TC1 was also negligible. However, the precipitation pattern of the TCs changed, which will be explained in later sections.

Table 4.3.: Average 6-hourly precipitation of the simulated TCs in different simulations between the first time step after seeding and the time step of landfall (TC1) or extratropical transition (TC2). The precipitation is averaged within 5° from the centre of the TC.

Simulation	Average precipitation (mm/6h)
CTRL (TC1)	178.27
L46E	177.52
L46W	177.34
L35E	177.37
L29E	177.73
CTRL (TC2)	202.40
L46S	203.06

4.3. Detailed Analysis

4.3.1. Initial Development of TC1

Based on the similarity in the intensity evolution in the different perturbation simulations shown in Figures 4.6a and 4.6b, one may have the perception that the CCN in the different simulations behaved in a similar manner. The intensity difference, compared to the control TC, started to become significant only after $T_{seed}+030h$. In fact, the additional CCN in the perturbation simulations interacted with the TC, such that they attained a similar state by $T_{seed}+030h$, when the rapid intensification of the TC allowed the differentiation in intensity between the control simulation and the perturbation simulations.

Figure 4.7 shows the azimuthal average of cloud droplet number concentration (CDNC) in the seeding height group simulations shortly after seeding. The azimuthal average CDNC was very small before seeding, with $<0.2\,\text{cm}^{-3}$ everywhere (Figure A.1). It can be seen that an elevated CDNC appeared already at $T_{\text{seed}}+006\text{h}$ for the L46E simulation, predominantly within $0.5°$ from the storm centre. The height with highest droplet number concentration remained in the boundary layer. The elevated droplet number concentration extended from the surface to model level 22 (4900 m). This shows that the extra CCN effectively caused more cloud droplets to form, which were effectively brought upward by the updraft in the eyewall (Figure 4.8a).
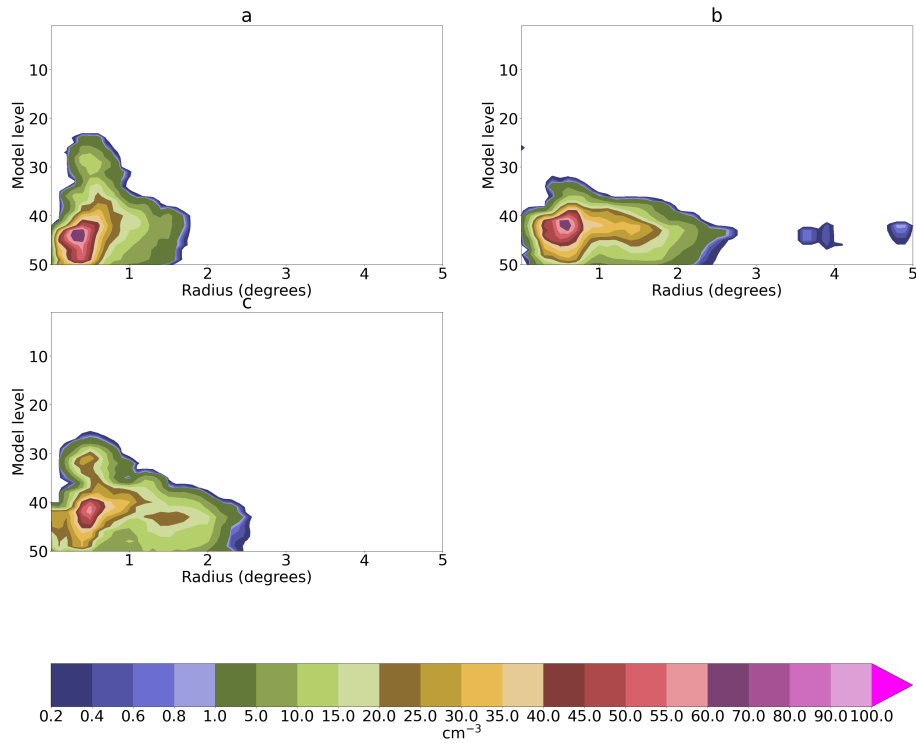
Figure 4.7.: Azimuthal average of CDNC in (a) the L46E simulation at $T_{\text{seed}}+006\text{h}$, (b) the L35E simulation at $T_{\text{seed}}+012\text{h}$ and (c) the 29E simulation at $T_{\text{seed}}+018\text{h}$. High values of CDNC were found mainly within $0.5°$ from the centre.

4. Results & Discussion

In the L35E and L29E simulations, similar patterns of CDNC as the L46E simulation could be observed, but the extra activated cloud droplets only appeared with a time lag with respect to the L46E simulation, at $T_{seed}+012h$ and $T_{seed}+018h$ respectively. The CDNC at earlier time steps is shown in Figure A.2. Moreover, the highest CDNC occurred below model level 40 (840 m), i.e., within the boundary layer, despite the extra CCN being injected at higher levels in these two simulations. The time lag in the formation of cloud droplets and the fact that the cloud droplets were mostly found in the boundary layer suggests that seeding CCN at upper levels was not able to activate cloud droplets there. Instead, they sank to the boundary layer with ample moisture to activate droplets. Moreover, cloud droplets were mainly activated near the eyewall instead of near the targeted seeding region, which was at least 2° away from the centre. This indicates that most of the extra CCN followed the inflow in the boundary layer and only activated cloud droplets near the eyewall where the air was the moistest (Figure 4.8b) and was forced to rise upwards, causing the most effective cloud droplet activation.

a   b
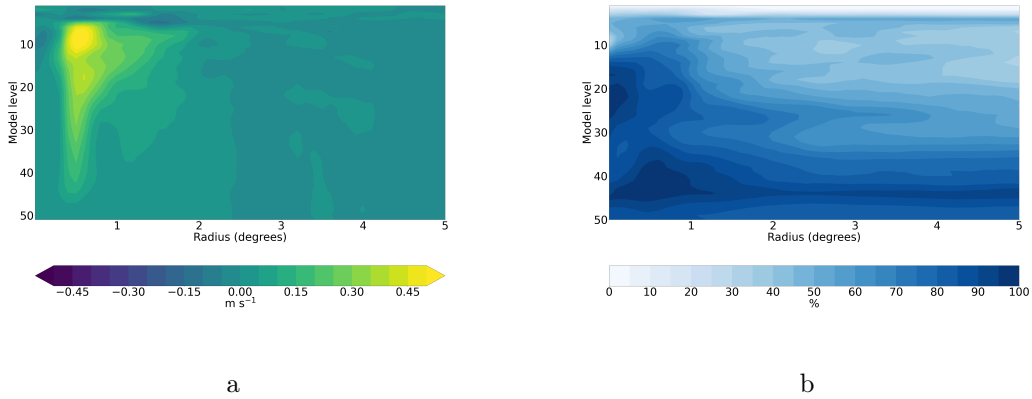
Figure 4.8.: Azimuthal average of (a) vertical velocity and (b) relative humidity in the L46E simulation at $T_{seed}+006h$.

In the L46W simulation, the boundary layer was seeded as for the L46E simulation, but on the western side of TC1. Figure 4.9 shows the cross section plots of CDNC at $T_{seed}+006h$ in the L46E and L46W simulations. Both simulations show elevated CDNC on both the west and the east of the centre of TC1. However, the concentration in the

L46W simulation was considerably lower than that in the L46E simulation. This can be explained by the asymmetry of TC1 at the start of seeding, which can be seen in Figure 4.10. The updraft in TC1 was asymmetric, in which the eastern eyewall had a sustained strong updraft throughout different heights in the TC. The western quadrant was relatively weak, with strong updrafts ($>0.4\,\mathrm{m\,s^{-1}}$) mainly confined in upper levels. Within the boundary layer, only isolated weak updrafts were found. There was even a strong downburst tongue extending from model level 20 ($5600\,\mathrm{m}$) downward, reaching the boundary layer. This was unfavourable for the formation of cloud droplets as a weak updraft or even a downdraft slows down the growth of supersaturation and therefore inhibits activation of droplets.
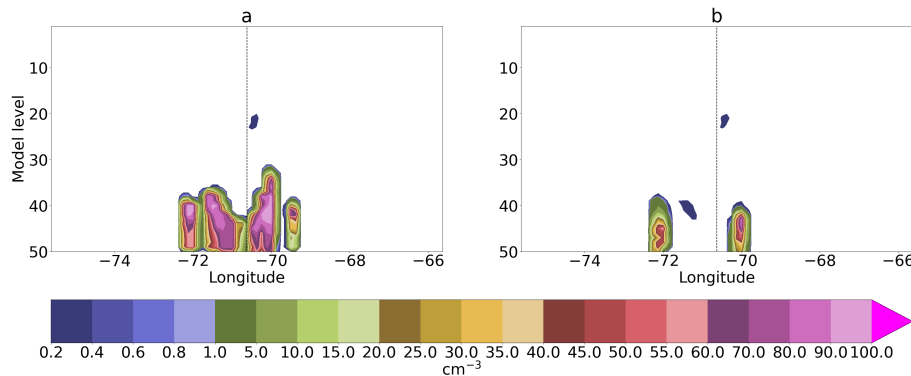
Figure 4.9.: Cross section of CDNC in (a) the L46E simulation and (b) the L46W simulation at $\mathrm{T_{seed}}$+006h. It can be seen that there were much more cloud droplets activated in the L46E simulation than in the L46S simulation at $\mathrm{T_{seed}}$+006h.

Nevertheless, the CDNC was approximately axisymmetric, which suggests that the CCN or the cloud droplets were advected with the cyclonic flow in both the L46E and L46W simulations shortly after seeding. In the L46E simulation, droplets were readily activated due to ample supersaturation from the updraft. Some of these droplets then followed the cyclonic flow of the TC and arrived at the western quadrant. In the L46W simulation, the formation of cloud droplets was suppressed at the western flank of TC1, thereby limiting the concentration of droplets there (and possibly at the eastern flank when they were advected by the flow). It was also possible that some CCN did not

form droplets at the western flank but were advected to the eastern flank where the environment was more conducive for droplet formation. The extra time required to transport the CCN might also explain the lower CDNC in the L46W simulation.
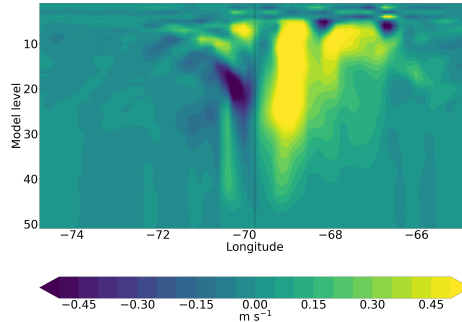

Figure 4.10.: Cross section of vertical velocity along the latitude of the centre of TC1 at T_{seed}. The black dashed vertical line marks the longitude of the TC centre. The updraft structure was asymmetric, with strong updrafts only on the east.

By $T_{seed}+030h$, the injected CCN in all TC1 simulations could eventually circulate around the TC. The updraft in the eyewall also became more axisymmetric. Thereby, the structure of the storm in the different simulations became similar, leading to a similar subsequent development of the TC.

4.3.2. Hovmöller Analysis

In order to visualise the development of the TC in its eye, its eyewall and the far-field region, Hovmöller diagrams of the eye, the eyewall and the far-field region were produced. The extent of the eye, the eyewall and the far-field region was defined from the azimuthal average of vertical velocity, averaged over the time between seeding and landfall of TC1 or extratropical transition of TC2. Upon time averaging, the structure of the azimuthal average vertical velocity was quite similar for the control simulation and the perturbation simulation(s). The time averaged azimuthal average plots of vertical velocity of the control and L46E simulations of TC1 and the control and L46S simulations

of TC2 are shown in Figure 4.11. The corresponding plots for the other TC1 perturbation simulations are shown in Figure A.3. For TC1, the eyewall region was defined to be between 0.2° and 0.9° from the TC centre, where the strongest updraft was found, with the eye within 0.2° from the TC centre. The region between 0.9° and 2.5° from the centre was defined as the far-field region, which was covered by the anvils of the eyewall updraft. The updraft structure of TC2 was similar, albeit considerably weaker than that of TC1. Therefore, the same boundary definitions were adopted for the Hovmöller analyses of TC2.
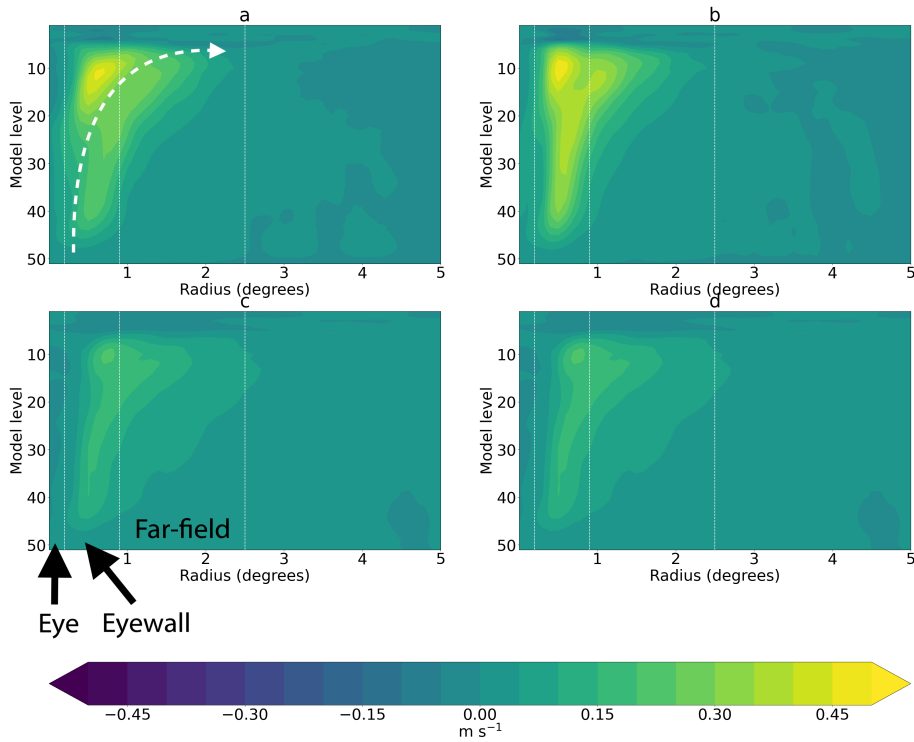
Figure 4.11.: Azimuthal average of vertical velocity in (a) the CTRL simulation of TC1, (b) the L46E simulation of TC1, (c) the CTRL simulation of TC2 and (d) the L46S simulation of TC2, averaged between T_{seed} and time of landfall (TC1, i.e., (a) and (b)) or extratropical transition (TC2, i.e., (c) and (d)). White vertical dashed lines mark the defined eye, eyewall and far-field regions in the Hovmöller analyses. The dotted arrow in panel (a) illustrates the eyewall updraft reaching the tropopause, diverging into the outflow and forming the anvil.

4.3.3. Subsequent Rapid Intensification of TC1

As the behaviour of the perturbed TC in different seeding simulations after T_{seed}+030h was similar, the subsequent development of TC1 is exemplified with the L46E simulation.

A phase of rapid intensification occurred in the perturbation simulations on 1 Sep, during which the decrease in surface pressure was much faster and the maximum wind speed increased more rapidly than the control simulation (T_{seed}+030h to T_{seed}+060h). To understand why TC1 intensified quicker when extra CCN were injected than in the control simulation, we first investigate the vertical velocity anomaly associated with the seeding. Figure 4.12 shows the Hovmöller diagram of the vertical velocity difference in the L46E simulation. A stronger updraft anomaly is clearly observed in the eyewall on 1 Sep, with the strongest anomaly occurring at the tropopause. A negative vertical velocity anomaly can be seen in the far-field region. This indicates that upward motion was further reinforced in the eyewall, while it was suppressed in the far-field region. The negative anomaly in the far-field region could also be associated with the downdraft brought by the eyewall convection. The negative anomaly in the far-field region had a smaller magnitude than the positive anomaly in the eyewall. This can be explained by mass continuity as the eyewall updraft was restricted to a small areal extent, but the compensating sinking motion occurred at a larger scale in the far-field.

Figure 4.13 shows a significant thickening of cloud cover above model level 20 (5600 m) on 1 Sep (T_{seed}+030h to T_{seed}+054h). The enhanced cloud cover even extended to model level 2 (18 700 m). The stronger updraft in the eyewall allowed cloud droplets to be carried to greater altitudes where they could freeze and release extra latent heat, thereby further enhancing buoyancy and favouring more vigorous convection. Clouds were also able to extend further up in the atmosphere, where the temperature was even lower. Besides, the enhanced cloud cover in upper levels could also be related to the enhanced moisture uptake at the surface, such that more hydrometeors could form at higher altitudes.
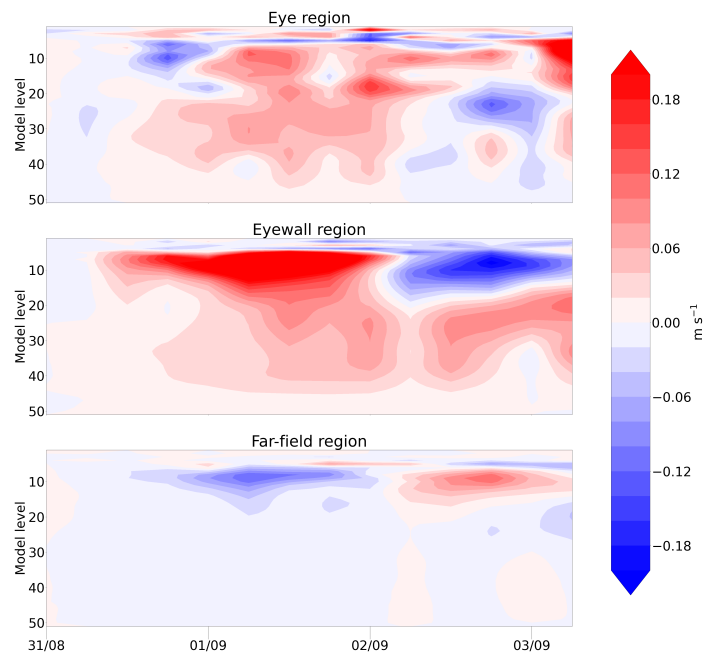
Figure 4.12.: Hovmöller diagram of vertical velocity difference in the L46E simulation. A significant updraft anomaly can be seen in the eyewall especially at the tropopause during the rapid intensification of TC1, while there was a negative anomaly in the far-field region.
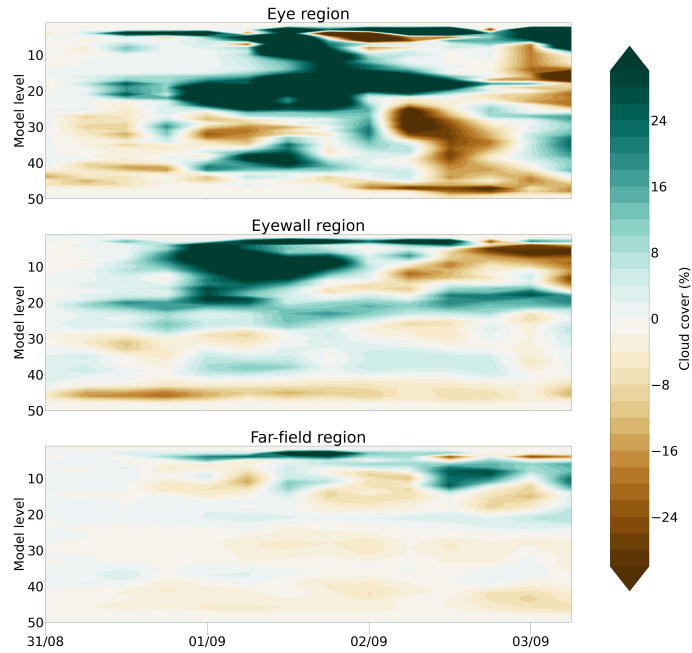
Figure 4.13.: Hovmöller diagram of cloud cover difference in the L46E simulation. The eye and the eyewall were significantly cloudier at the tropopause. The boundary layer cloud cover decreased throughout the TC due to stronger cloud lifting.

From the perspective of the Carnot cycle, the air reaching colder temperature at the cold reservoir, i.e., the tropopause, led to an enhancement in the thermal efficiency and therefore an increase in work done in the TC. From Figure 4.14, it is also observed that there was more ice forming at the freezing levels. This is because of the strengthened eyewall updraft as well as the significantly elevated CDNC, which hinted at a reduced droplet size. The delayed collision and coalescence process allowed liquid droplets to be lifted to freezing levels and to release more latent heat upon freezing, favouring even stronger updrafts. By mass continuity, the flux at the surface into the eyewall became stronger, which implies a higher wind speed.
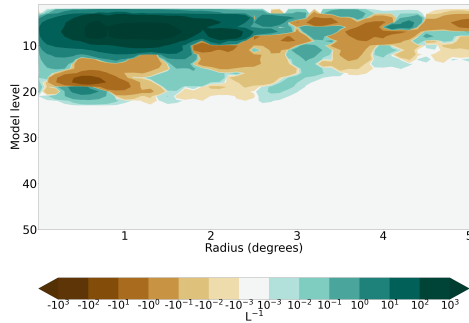
Figure 4.14.: Azimuthal average of ice crystal number concentration difference in the L46E simulation at $T_{seed}+036h$. Note that log scale is used in the plot. There were many more ice crystal at the tropopause in the eyewall, while there was a band of decreased ice crystal number concentration below.

It is also seen that the eye became cloudier especially in the lower levels and the upper levels. This was related to a change in the moisture distribution in TC1. Figure 4.15 shows the Hovmöller diagram of θ_e difference in the L46E simulation. On 1 Sep, a warm anomaly was seen in the eyewall in the lower levels and at the tropopause, while there was an apparent cold anomaly in mid-levels. The warm anomaly was also present in the eye and the far-field region in lower levels. This indicates enhanced moisture uptake of TC1, as the availability of extra CCN promoted droplet formation. The moisture even intruded the eye of TC1, as suggested by Figure 4.7, where the cloud droplets edged very close to the centre of TC1. This was probably due to the immaturity of the eye of TC1 during seeding, such that the eye dynamics were not strong enough to counter the surface inflow. The cold anomaly in the eyewall was partly due to delayed freezing where the droplets did not freeze at the mid-levels but were brought to higher levels. This can be seen in Figure 4.14, where there was a band of decreased ice crystal number concentration right below a band of increased ice crystal number concentration. Another reason for the cold anomaly was the displacement of the eyewall updraft between the control and perturbation simulations. As shown in Figure 4.16, the updraft in the L46E simulation was more vertical, while that in the control simulation slanted outward with height. This
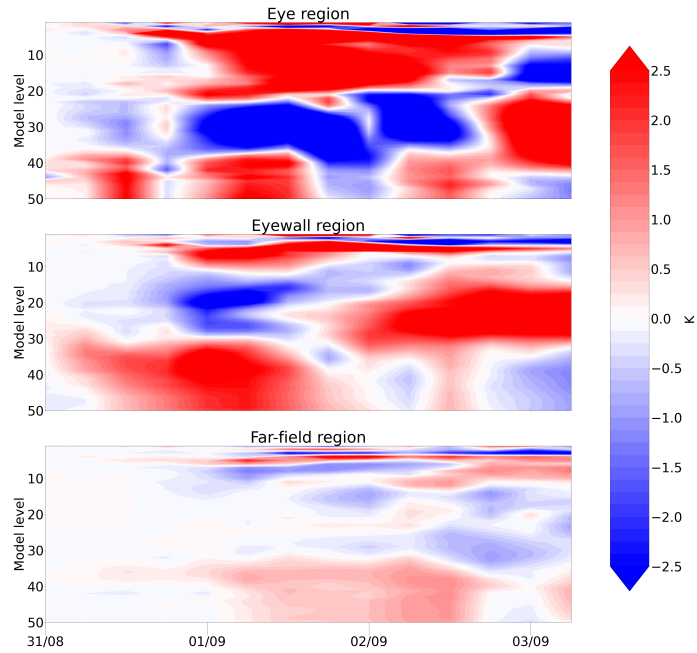
Figure 4.15.: Hovmöller diagram of θ_e difference in the L46E simulation. The eye and the eyewall became significantly warmer in lower levels and upper levels because of enhanced moisture uptake and release of latent heat of fusion respectively.

could lead to an illusion of a dry and cold anomaly in the L46E simulation where the outward-slanting eyewall of the control TC was situated at, and could explain the cold anomaly seen in the eyewall region in Figure 4.15. The warm anomaly at the tropopause was due to enhanced latent heat release through freezing. The enhanced moisture uptake at the surface also contributed to higher θ_e values at the tropopause through adiabatic expansion in the eyewall updraft. In the far-field, a slight warm anomaly developed on 1 Sep. This indicates an enhanced moisture uptake due to the abundance of CCN.

In the eye of TC1, there was also a warm anomaly in θ_e at the tropopause and a cold anomaly in mid-levels. The enhanced eyewall updraft caused stronger divergence at the tropopause. The air arriving at the tropopause did not only accelerate outward (as in
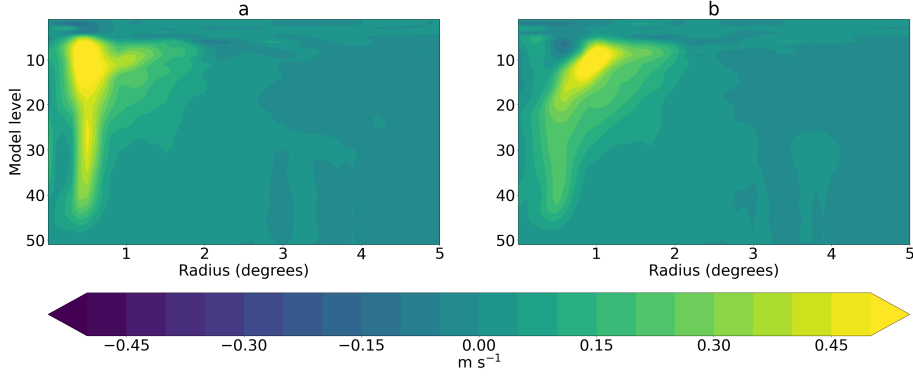
Figure 4.16.: Azimuthal average of vertical velocity in (a) the L46E simulation and (b) the CTRL simulation of TC1 at T_{seed}+036h. The eyewall updraft in the L46E simulation was more vertical while that in the control simulation slanted outwards with height.

the adiabatic cooling branch in the Carnot cycle as shown in Figure 1.4), but some air was also pushed into the eye. The air was of high θ_e as it contained a lot of moisture, and released extra latent heat at the tropopause when the cloud droplets froze. The cold anomaly below was due to evaporative cooling as the air containing hydrometeors subsided in the eye. These hydrometeors melted and evaporated as the air sank and warmed, leading to consumption of latent heat and therefore cooling of the air. The Hovmöller diagrams of vertical velocity, cloud cover and θ_e differences of the L35E, L29E and L46W simulations are shown in Figure A.4. The plots of their azimuthal average of ice crystal number concentration and vertical velocity are shown in Figures A.5 and A.6 respectively. It can be seen that they had a similar development as in the L46E simulation following the seeding.

Due to the changed moisture distribution, the precipitation pattern also changed. Figure 4.17 shows the precipitation difference in the L46E simulation at T_{seed}+030h and T_{seed}+054h respectively. These two time steps were chosen because the control and perturbed storms were at the same grid point, such that the precipitation signals were not masked by noises due to displacement. At T_{seed}+030h, the precipitation difference shows an annular structure, with enhanced precipitation close to the centre and suppressed

precipitation at slightly larger radii. This is because there was enhanced moisture uptake with vigorous convection in the eyewall, which led to enhanced rainfall. At larger radii, despite the enhanced moisture uptake as indicated by higher values of θ_e, convection was suppressed. Furthermore, the updraft in the far-field region was weak, such that the reduction in droplet size dominated and hindered the cloud droplets to grow in size to precipitate out. At $T_{seed}+054h$, the difference signals became stronger, but changed into a dipole structure, with enhanced precipitation near the centre and tailing towards the east and suppressed precipitation to the north. The tail towards the east was due to the westward movement of the TC. The dipole structure could be due to individual rainband development, such that the signal to the south was masked. Nevertheless, the pattern still shows that precipitation was enhanced in the eyewall and was hindered in the far-field region. The corresponding precipitation difference plots in the L35E, L29E and L46W simulations are shown in Figure A.7, which shows a similar change in precipitation pattern as in the L46E simulation.
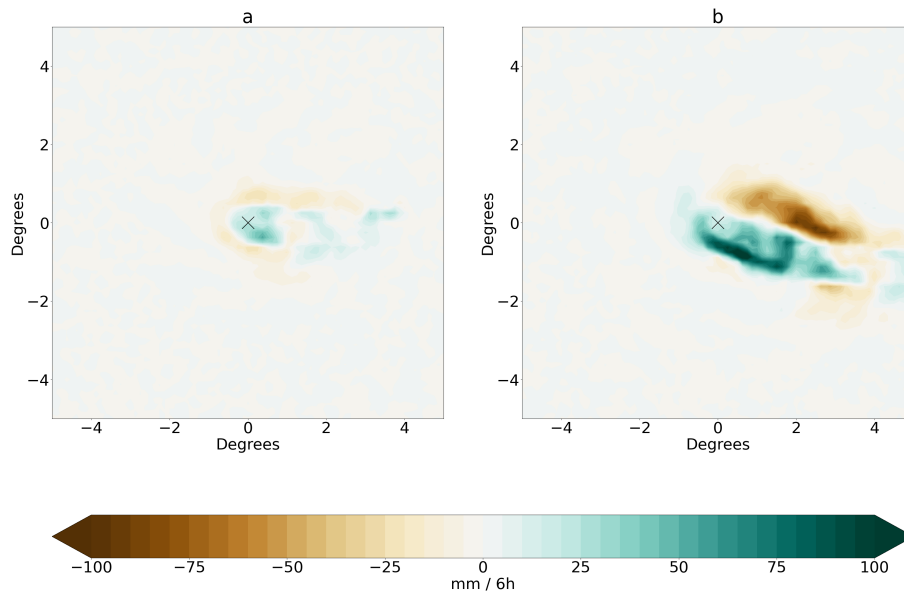
Figure 4.17.: Total precipitation difference in the L46E simulation at (a) T_{seed}+030h and (b) T_{seed}+054h. The black cross marks the origin and shows the centre of TC1. Difference was calculated by overlapping the TC centres in the respective simulations. It can be seen that there was enhanced precipitation close to the centre and suppressed precipitation at larger radii.

4.3.4. Development of TC2 and Comparison with TC1

Figure 4.18 shows the CDNC in the L46S simulation 6, 24 and 48 hours after seeding respectively. Similar to that in TC1, the azimuthal average CDNC was very small before seeding, with $<0.2\,\mathrm{cm}^{-3}$ everywhere (Figure A.1). The injected CCN in TC2 also helped to increase the CDNC in TC2. Nevertheless, the distribution of these cloud droplets was different from that in TC1. It can be seen that a primary maximum still occurred very close to the centre, i.e., about 0.5° from the TC centre. However, unlike TC1, in which the strong mass convergence caused high values of CDNC to be concentrated near the eyewall (Figure 4.19 for the L46E simulation, Figure A.8 for the L35E, L29E and L46W simulations), many cloud droplets in the L46S simulation still remained at larger radii. This indicates that the boundary layer inflow was not very strong, such that not all seeded CCN were transported into the eyewall and could activate more cloud droplets in the far-field. This weakened the warm rain suppression effect in the eyewall, because the reduction in amount of available CCN in the eyewall led to faster growth of droplets due to less competition of water vapour. The droplets could rain out earlier without reaching freezing levels, such that they were unable to release extra latent heat by freezing.
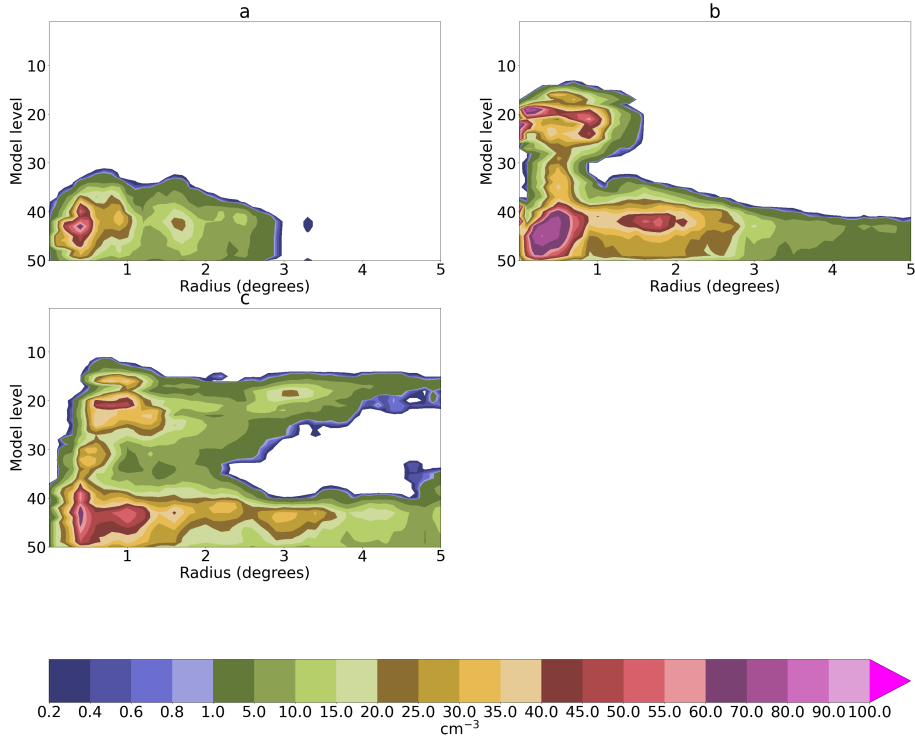
Figure 4.18.: Azimuthal average of CDNC in the L46S simulation at (a) T_{seed}+006h, (b) T_{seed}+024h and (c) T_{seed}+048h. The primary maximum in lower levels was within about 0.5° from the centre but high values of CDNC are observed also at larger radii. The anvil structure in panel (c) indicates that at least a part of the TC outflow is below the freezing levels.
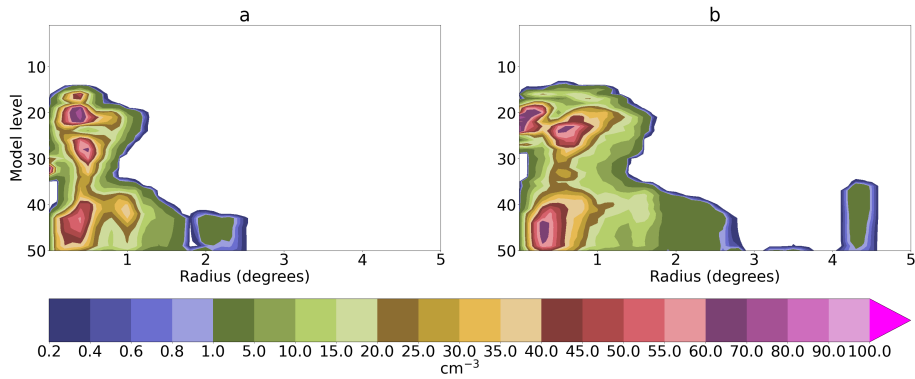

Figure 4.19.: Azimuthal average of CDNC in the L46E simulation at (a) T_{seed}+024h and (b) T_{seed}+048h. High values of CDNC were mostly confined close to the centre.

43

Figure 4.20 shows the Hovmöller diagram of θ_e in the L46S simulation. It can be seen that the warm anomaly in the eyewall was less intense than that in the L46E simulation (Figure 4.15). This indicates that there was relatively less moisture transport into the eyewall. The moist inflow partly remained in the far-field region, in which it became slightly warmer in lower levels. However, the extra cloud droplets formed in the far-field region were not able to reach freezing levels to weaken the eyewall by the mechanism illustrated in Figure 1.5, because the elevated CDNC in the far-field region were confined to lower levels. This shows that there should be little extra ice forming in the outer clouds compared to the control simulation.
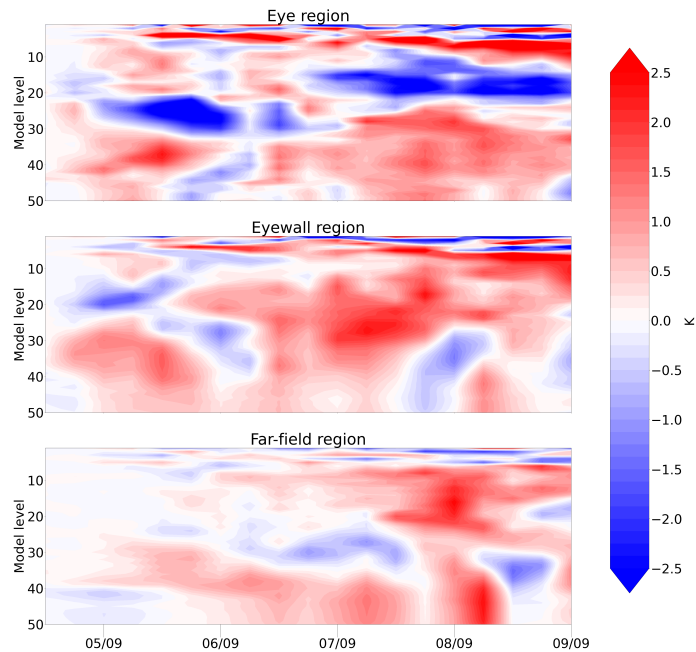

Figure 4.20.: Hovmöller diagram of θ_e difference in the L46S simulation. There was a warm anomaly in the eyewall due to enhanced moisture uptake, but the warming was less significant than that in the L46E simulation.

4. Results & Discussion

Comparing Figures 4.18 and 4.19, we see that the high CDNC in the eyewall updraft in the L46E simulation mainly extended vertically to the upper levels (until above where the droplets should freeze). Whereas the L46S simulation shows an anvil structure, where the high CDNC spread outward in upper levels. This resembles the structure of the TC outflow and indicates (at least a part of) the TC2 outflow in the L46S simulation occurred below freezing levels. This means that these cloud droplets did not have the chance to rise further up to freeze to release extra latent heat. Figure 4.21 shows the azimuthal average of specific cloud ice content in the L46E and L46S simulations at $T_{seed}+048h$ respectively. The corresponding plots in the L35E, L29E and L46W simulations are shown in Figure A.9. Figure 4.21 illustrates that TC2 in the L46S simulation had much less ice than TC1 in the L46E simulation, as there was less buoyancy due to freezing of cloud droplets in the L46S simulation. This is because more moisture remained in the far-field region. Furthermore, the weaker mass convergence in TC2 caused less seeded CCN to be advected towards the eyewall, which fostered faster growth of droplets in the eyewall and they were more likely to be precipitated out before reaching freezing levels. A feedback loop was established where less cloud droplets could freeze, further hindering the updraft enhancement and droplet freezing. Whereas for TC1 in the L46E simulation, there was extensive freezing since more smaller droplets hindered early rain out. The updraft was further enhanced, enabling cloud droplets to continuously be carried to upper levels to freeze. A strong updraft was able to sustain through the cycle and allowed TC1 to further intensify. It is also seen from Figure 4.22 that strengthening of the updraft in the L46S simulation is weaker than that in the L46E simulation (Figure 4.12) especially in upper levels, which also explained why the decrease in surface pressure in TC2 in the L46S simulation was less significant than that in TC1 in its perturbation simulations.

Furthermore, TC1 having an outflow at higher altitudes in the L46E simulation, compared to TC2 in the L46S simulation, indicates a larger enhancement in the Carnot efficiency, as the outflow reached colder temperatures. This demonstrates that the energy extracted from the ocean was more efficiently utilised in the L46E simulation and favoured the higher intensity of the TC.

45

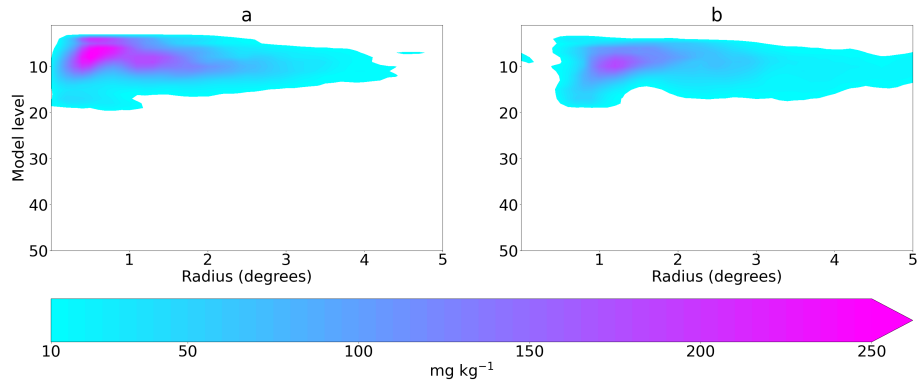Figure 4.21.: Azimuthal average of specific cloud ice content in (a) the L46E simulation and (b) the L46S simulation at $T_{seed}+048h$. There was higher specific cloud ice content at the tropopause in the eyewall in the L46E simulation than in the L46S simulation.
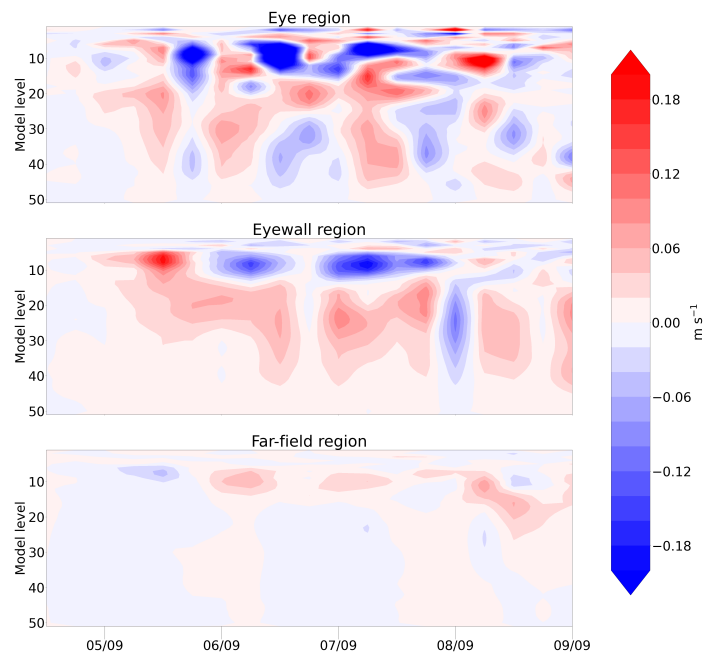

Figure 4.22.: Hovmöller diagram of vertical velocity difference in the L46S simulation. There was an updraft anomaly in the eyewall but it was less significant than in the L46E simulation.

46

4. Results & Discussion

In terms of cloud structure, the effects of seeding in TC2 were not the same as in TC1. It can be seen from Figure 4.23 that the cloud cover in the boundary layer in the eyewall decreased, which was similar to that in TC1, because there was an enhanced updraft in both cases compared to their respective control simulation, which caused more lifting. On one hand, the were more mid-level clouds in the eyewall, because of an enhanced moisture uptake due to abundance of CCN compared to the control simulation. On the other hand, the cloud cover at the tropopause in the eyewall did not significantly increase. This is because the cloud droplets have possibly precipitated out or went into the outflow before reaching the tropopause. Within the eye, the change in cloud cover was much less significant than that in the L46E simulation. The reasons behind were the weaker eyewall divergence and possibly stronger eye dynamics. As indicated in Figure 4.22, the eyewall updraft in the L46S simulation strengthened less than that in the L46E simulation. Thereby, there would be a weaker divergence at the tropopause, such that there should be less flow carrying abundant hydrometeors into the eye. Moreover, the eye of TC2 was better defined since T_{seed}. This indicates that the eye dynamics of TC2 were stronger, such that the TC was able to maintain a cloud-free eye. In contrast, the eye of TC1 was not well defined, implying the eye dynamics could not sustain a clear eye. The extra hydrometeors from the strong eyewall updraft could have been carried into the eye, or the surface flux was stronger than the rate of subsidence, resulting in a cloudy eye.
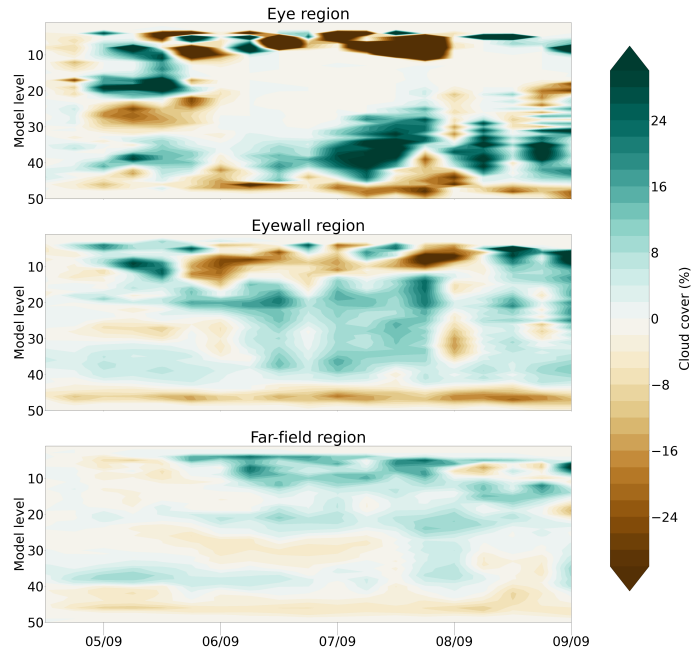
Figure 4.23.: Hovmöller diagram of cloud cover difference in the L46S simulation. The boundary layer cloud cover decreased due to stronger cloud lifting. The change in cloud cover in the eye was much less significant than in the L46E simulation.

The precipitation pattern also changed in TC2. The total precipitation difference plots at $T_{seed}+030h$ and $T_{seed}+054h$, when there was no displacement between the control and perturbation simulations, are shown in Figure 4.24. At $T_{seed}+030h$ and $T_{seed}+054h$, TC2 was moving northward and northeastward respectively. At $T_{seed}+030h$, there was a slight negative anomaly to the east of TC2, with a more compact slight positive anomaly closer to the centre. The signal at $T_{seed}+054h$ is stronger, with negative anomalies to the east of the TC centre and braiding towards the southwest. A positive anomaly was again found around the centre and also tailing towards the southwest because of the TC's northeastward movement. The patterns in both figures resemble the dipole structure as in the L46E simulation of TC1 at $T_{seed}+054h$ (Figure 4.17). This implies that the

precipitation in TC2 was influenced by the injected CCN in a similar manner as in TC1 as explained previously. The precipitation close to the centre was enhanced due to stronger convection and enhanced moisture content. At larger radii, the weak updraft together with the reduced droplet size hindered the formation of precipitation. The dipole signal is in general weaker in TC2 than in TC1, because the eyewall updraft was less enhanced and less moisture was picked up.
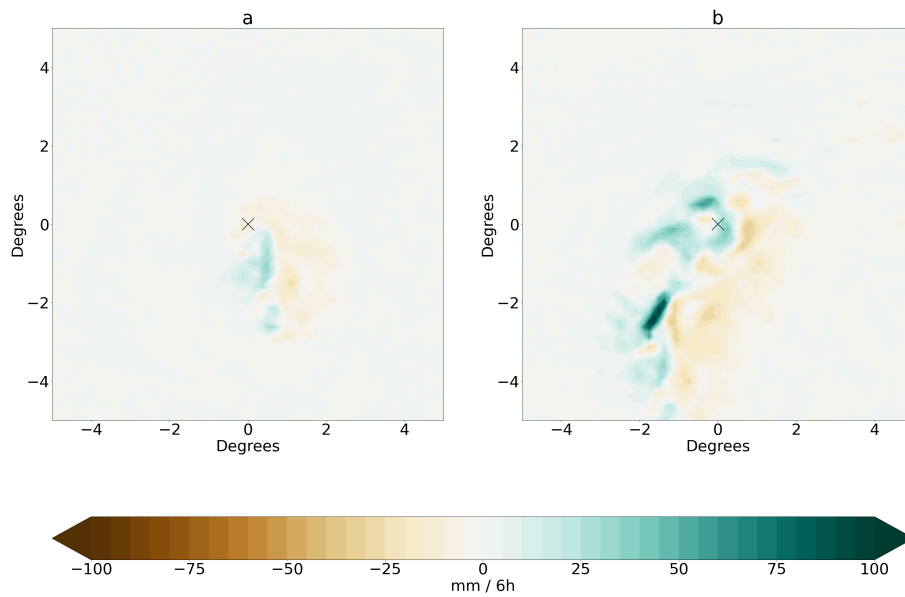

Figure 4.24.: Total precipitation difference in the L46S simulation at (a) T_{seed}+030h and (b) T_{seed}+054h. The black cross marks the origin and shows the centre of TC2. Difference was calculated by overlapping the TC centres in the respective simulations. A dipole structure, with enhanced precipitation close to the centre and suppressed precipitation further to the east, is observed, but the dipole signal is weaker than that in the L46E simulation.

4.4. Discussion

The results of the perturbation simulations in both TCs show that the weakening of TC by invigoration of convection in the outer rainbands, as suggested by different studies including Zhang et al. (2009) and Hazra et al. (2013), were not achieved in our study. The difference between their and our results may be attributed to the different model configurations, in which they had nested domains with fine resolutions, while we had a horizontal resolution of 13 km in the whole domain. Furthermore, the methods of seeding are different. They specified a horizontally homogeneous layer with high CCN concentration surrounding the TC, in order to examine the microphysical responses of the TC in extreme scenarios. This is hardly achievable in reality compared to our simulations, in which we targeted specific areas in the TC for seeding.

Instead, our simulation results agree with that of Herbener et al. (2014) and Liang et al. (2021). The seeded CCN in all of our perturbation simulations were eventually advected towards the eyewall, despite a slight difference in the timing and the proportion, which depended on the seeding altitude and the mass convergence in the TC. As suggested by Liang et al. (2021), even though there were more CCN in both the eyewall and the far-field region (especially in TC2 where the mass convergence was weaker), the eyewall convection was invigorated because of the stronger updrafts there, while the convection in the far-field region was suppressed. Furthermore, the stretching effect which spins up the TC as hypothesised by Herbener et al. (2014) was also apparent in our simulations, in which TC1 intensified more and reached higher wind speed than TC2 when seeded with CCN, as the eyewall clouds in TC1 reached higher altitudes than those in TC2 because of greater buoyancy.

From the Hovmöller diagrams of θ_e difference in our simulations, we see a slight cold anomaly in the boundary layer in the far-field region initially, which was later replaced by a slight warm anomaly. The effect suggested by Herbener et al. (2014), by which environmental air with lower θ_e is being drawn into the storm, is not prominently seen in our simulations. This is because the abundance of CCN, part of which remained in

the far-field region, facilitated cloud droplet formation, during which the air gained in moisture as well as θ_e, and cancelled out the effect of possible cool environmental air intrusion.

Cotton et al. (2012) and Rosenfeld et al. (2012) speculated CCN intrusion into a weak and poorly organised TC may aid its intensification initially because there was little convection invigoration of spiral rainbands, such that the CCN could invigorate the eyewall convection. Comparing our TC1 and TC2 simulations, in which the former had a poorer structure than the latter at T_{seed}, we see a distinct rapid intensification in TC1 but not in TC2. We attribute the difference mainly to the difference in mass convergence. Given the difference in the TC's structures, their theory may also plausibly play a part in the evolution of the TCs in our simulations. However, our results disagree with the latter part of the theory of Cotton et al. (2012), which stated that the initial intensification was followed by weakening. We believe this is because the initial intensification caused the eyewall updraft to substantially strengthen with the feedback cycle (especially in TC1), such that any development of the outer rainbands which could weaken the eyewall was suppressed.

In contrast to the results of Jiang et al. (2016), which suggested a lower precipitation rate due to smaller droplet size upon seeding, our results indicate that there was no significant change in the total precipitation of the TC. This could be due to an enhanced moisture uptake which cancelled out their hypothesised effect. The change in precipitation patterns in our simulations also disagrees with that of Zhao et al. (2018), which suggested an enhancement in precipitation in the outer rainbands following the convection invigoration there. Our results show that the eyewall precipitation was enhanced while the precipitation at larger radii was suppressed, because the eyewall convection did not weaken but strengthened instead.

In terms of TC tracks, our results agree with the results of previous studies (W. Lin et al., 2011; Cotton et al., 2012; Jiang et al., 2016; Liang et al., 2021), which stated that there was no significant change in the TC tracks. This is because the perturbation caused by the injection of CCN is too small to disrupt the large-scale steering flow.

5. Limitations, Conclusion & Outlook

5.1. Limitations

The injection of extra CCN in the ICON model led to a perturbed TC development. Yet, there are several limitations in the method that should be recognised.

Firstly, there were only two TCs being seeded in the research, and they do not represent all possible characteristics of all TCs. The two TCs mainly differed in the cloud structure and the intensity development trend, which led to differences in their response to seeding and helped to understand how TCs react to extra CCN. The TCs were only seeded at one specified stage of development. They could have developed differently, if they were seeded at another stage of development, e.g., during cyclogenesis or during their intensity peak.

Secondly, the Hovmöller analyses were not rigorous enough, as the eye, eyewall and far-field regions were defined based on a time-averaged vertical velocity for simplicity. During the life cycle of a TC, its structure could change. For instance, the eyewall would contract as the TC intensifies. A double eyewall could also appear if the eyewall replacement cycle occurs, which is typical in intense TCs. Moreover, eyewalls typically slant outwards with height, such that defining the eyewall region in a vertical manner is not entirely realistic. The simplified analysis would mask the signals in the Hovmöller analyses. A more rigorous analysis could be done by defining the three regions at each time step separately.

Thirdly, the tracks of the TCs were changed, albeit insignificantly, upon the seeding. There could be a change in the ocean conditions which may influence the TC's development and may have masked the signals due to cloud physics.

Moreover, the seeding box targeting the outer rainbands of the TC covered the strongest part of the rainbands but barely resembled the structure of the rainbands. The behaviour of these "excess" CCN not seeding the outer rainbands could interfere with the effect that was hypothesised to be achieved, i.e., to weaken the TC by invigorating the convection

at the outer rainbands. Besides, the seeding was applied for one hour over the same area. The movement of the TC and its own development may cause the area of the seeding box to deviate from the targeted rainbands. In a more realistic setup, the seeding box should move with the TC, or ideally with the rainbands. In addition, our seeding box spanned an area of $3° \times 3°$. It is questionable if this is technologically executable in reality, such that our simulation results are not directly comparable with reality.

In our simulations, the sea surface temperature was prescribed as the monthly mean. In reality, there is strong ocean-atmosphere coupling in a TC. For instance, TCs consume energy from the warm ocean water and the fierce winds cause vigorous mixing of ocean water, possibly stirring up deep cold water in the ocean. This could possibly inhibit the intensification of TCs and is most prominent when the TC is slow-moving. Furthermore, fierce winds contribute to rough sea conditions, where sea salt aerosols could be generated from the high waves and could act as giant CCN, which may further alter the cloud physics in the TC.

5.2. Conclusion & Outlook

In this study, two TCs over the North Atlantic were simulated. CCN were injected in designated areas, targeting the outer rainbands or mimicking TCs intersecting aerosol sources. In TC1, simulations with seeding at different heights targeting an outer rainband, as well as a simulation imitating the TC intersecting aerosol sources were performed. For TC2, CCN were injected targeting its outer rainband, aiming at comparing the impacts of CCN in TCs with different structures.

The simulation results show that the CCN injected in the TC were advected by the radial inflow in the boundary layer towards the eyewall, even if they were injected at greater heights where the inflow was weak. CCN seeded at greater heights sank into the boundary layer. Convection was barely invigorated in the outer rainbands or in regions lacking convection due to weak updraft compared to that in the eyewall. Instead, the CCN enhanced moisture uptake and was brought to upper levels by the eyewall

updraft. Due to the competition of water vapour, the droplet growth rate was impeded, such that the droplets did not grow fast enough and were less likely to precipitate out before reaching the freezing levels. Upon freezing, they released latent heat and enhanced buoyancy, further reinforcing the eyewall updraft. This created a feedback cycle, as the stronger eyewall updraft favoured even more droplets to reach the freezing levels. By mass continuity, the inflow in the boundary layer was enhanced, leading to an increase in wind speed.

The above feedback cycle was dependent on the mass convergence in the TC. At T_{seed}, TC1 was on an intensifying trend, such that the mass convergence was stronger, advecting the seeded CCN towards the eyewall more effectively. The feedback cycle was stronger, which caused TC1 to subsequently rapidly intensify and attained a higher intensity than in the control simulation. The intensification trend in TC2 was stalled during seeding. The mass convergence was therefore weaker, such that the invigoration of convection in the eyewall was less prominent. There was relatively less enhancement in intensity compared to TC1.

The extra buoyancy in TC1 also caused the air in the eyewall updraft to reach further higher in the atmosphere, where the hydrometeors froze. This caused an enhancement in cloud cover at the tropopause in the eyewall. The vigorous eyewall updraft in TC1 also implies a strong inflow in the boundary layer and strong divergence at the tropopause. Since the eye of TC1 was not well developed, moist air from the eyewall updraft and from the boundary layer intruded the eye at the tropopause and in the boundary layer respectively, leading to a thickening of cloud cover there and a turbid eye. Whereas in TC2, the eye was clear, indicating strong eye dynamics, such that the cloud cover change in the eye was insignificant. Besides, there was a decrease in boundary layer cloud cover in both TCs predominantly in the eyewall because the enhanced updraft caused stronger cloud lifting.

The enhanced moisture uptake and the strengthened updraft caused enhanced precipitation in the eyewall, while there was less precipitation at larger radii. This is because the droplet size was reduced, and the updraft was weaker at larger radii, hindering the

formation of precipitation. The change in precipitation was more significant in TC1 because of the stronger updraft enhancement feedback. Finally, the injection of CCN caused no significant change in the tracks of the TCs.

Overall, the mechanisms with which the TC responds to the seeded CCN are manifold and are dependent on the TC structure and development. Looking ahead, simulations of TCs with different features could be done, as this could more realistically represent different TCs in reality. One should also consider using fully coupled ocean-atmosphere models for the simulations to best resemble reality. This should help to understand the potential impacts of the geoengineering approach, should a TC in reality be seeded with aerosols. However, it would also be advisable to simulate a idealised TC vortex or in an idealised environment in the interest of understanding the underlying cloud physics. One may also consider the use of ensemble modes in a model with slightly different initial and boundary conditions (and/or seeding configurations) to better assess possible outcomes of a TC seeding operation.

Acknowledgements

I would like express my sincere gratitude to Professor Ulrike Lohmann, the main supervisor of my thesis for her insightful and invaluable advice and suggestions on my project. Throughout every meeting and discussion with her, I have always been able to refresh and learn some new knowledge about tropical cyclones. She helped me a lot to understand and interpret the sophisticated results of the simulations, as well as to improve the writing and structure of my thesis. It would be impossible to complete the project without her guidance.

I would like to thank Ms. Nadja Omanovic, my co-supervisor, for the technical support and suggestions on the writing of the thesis. She provided a lot of useful guidance and many resources to help with the simulations, especially at the beginning when I was not familiar with the model configurations. She also provided inspiring comments on the interpretation of the results.

I wish to extend my thanks to all other group members in the Atmospheric Physics group for the valuable comments and feedback on my presentation. Their comments also helped the interpretation of the results and provided a possible future research direction for a better understanding on the interaction between TC and aerosols.

Finally, I would also like to thank my colleagues who are also working on their theses with me for their support and company in these fruitful six months.

6. References

Bell, G. D., Halpert, M. S., Schnell, R. C., Higgins, R. W., Lawrimore, J., Kousky, V. E., Tinker, R., Thiaw, W., Chelliah, M., & Artusa, A. (2000). Climate assessment for 1999. *Bulletin of the American Meteorological Society, 81*(6), S1–S50. https://doi.org/10.1175/1520-0477(2000)81[s1:CAF]2.0.CO;2

Braun, S. A. (2010). Reevaluating the role of the Saharan Air Layer in Atlantic tropical cyclogenesis and evolution. *Monthly Weather Review, 138*(6), 2007–2037. https://doi.org/10.1175/2009MWR3135.1

Carlson, T. N., & Prospero, J. M. (1972). The large-scale movement of Saharan air outbreaks over the Northern Equatorial Atlantic. *Journal of Applied Meteorology and Climatology, 11*(2), 283–297. https://doi.org/10.1175/1520-0450(1972)011<0283:TLSMOS>2.0.CO;2

Carrio, G. G., & Cotton, W. R. (2011). Investigations of aerosol impacts on hurricanes: Virtual seeding flights. *Atmospheric Chemistry and Physics, 11*(6), 2557–2567. https://doi.org/10.5194/acp-11-2557-2011

Cotton, W. R., Krall, G., & Carrió, G. (2012). Potential indirect effects of aerosol on tropical cyclone intensity: Convective fluxes and cold-pool activity. *Tropical Cyclone Research and Review, 1*(3), 293–306. https://doi.org/10.6057/2012TCRR03.05

Cotton, W. R., Pielke Sr, R., Walko, R., Liston, G., Tremback, C., Jiang, H., McAnelly, R., Harrington, J., Nicholls, M., Carrio, G., et al. (2003). RAMS 2001: Current status and future directions. *Meteorology and Atmospheric Physics, 82*(1), 5–29. https://doi.org/10.1007/s00703-001-0584-9

Cotton, W. R., Zhang, H., McFarquhar, G. M., & Saleeby, S. M. (2007). Should we consider polluting hurricanes to reduce their intensity? *The Journal of Weather Modification, 39*(1), 70–73. https://doi.org/10.54782/jwm.v39i1.204

Dunion, J. P., & Velden, C. S. (2004). The impact of the Saharan Air Layer on Atlantic tropical cyclone activity. *Bulletin of the American Meteorological Society, 85*(3), 353–366. https://doi.org/10.1175/BAMS-85-3-353

6. References

Emanuel, K., et al. (2003). Tropical cyclones. *Annual review of earth and planetary sciences*, *31*(1), 75–104. https://doi.org/10.1146/annurev.earth.31.100901.141259

Emanuel, K. (2005). Increasing destructiveness of tropical cyclones over the past 30 years. *Nature*, *436*(7051), 686–688. https://doi.org/10.1038/nature03906

Emanuel, K. (2006). Hurricanes: Tempests in a greenhouse. *Physics Today*, *59*(8), 74–75. https://doi.org/10.1063/1.2349743

Enz, B., Engelmann, J., & Lohmann, U. (2023, in press). Parallel use of threshold parameter variation for tropical cyclone tracking. *Geoscientific Model Development*. https://doi.org/10.5194/gmd-2022-279

Farfán, L. M., D'Sa, E. J., Liu, K.-b., & Rivera-Monroy, V. H. (2014). Tropical cyclone impacts on coastal regions: The case of the Yucatán and the Baja California Peninsulas, Mexico. *Estuaries and coasts*, *37*(6), 1388–1402. https://doi.org/10.1007/s12237-014-9797-2

Geiger, T., Frieler, K., & Bresch, D. N. (2018). A global historical data set of tropical cyclone exposure (TCE-DAT). *Earth System Science Data*, *10*(1), 185–194. https://doi.org/10.5194/essd-10-185-2018

Ghosh, S., Sharma, A., Arora, S., & Desouza, G. (2016). A geoengineering approach toward tackling tropical cyclones over the Bay of Bengal. *Atmospheric Science Letters*, *17*(3), 208–215. https://doi.org/10.1002/asl.644

Giorgetta, M. A., Brokopf, R., Crueger, T., Esch, M., Fiedler, S., Helmert, J., Hohenegger, C., Kornblueh, L., Köhler, M., Manzini, E., Mauritsen, T., Nam, C., Raddatz, T., Rast, S., Reinert, D., Sakradzija, M., Schmidt, H., Schneck, R., Schnur, R., . . . Stevens, B. (2018). ICON-A, the atmosphere component of the ICON earth system model: I. model description. *Journal of Advances in Modeling Earth Systems*, *10*(7), 1613–1637. https://doi.org/10.1029/2017MS001242

Greenspan, H. P., & Howard, L. N. (1963). On a time-dependent motion of a rotating fluid. *Journal of Fluid Mechanics*, *17*(3), 385–404. https://doi.org/10.1017/S0022112063001415

6. References

Grell, G. A., Peckham, S. E., Schmitz, R., McKeen, S. A., Frost, G., Skamarock, W. C., & Eder, B. (2005). Fully coupled "online" chemistry within the WRF model. *Atmospheric Environment*, *39*(37), 6957–6975. https://doi.org/10.1016/j.atmosenv. 2005.04.027

Halliday, D., Resnick, R., & Walker, J. (2014). *Fundamentals of physics* (10th edition). John Wiley & Sons.

Harper, B. A. (1999). Numerical modelling of extreme tropical cyclone winds. *Journal of Wind Engineering and Industrial Aerodynamics*, *83*(1), 35–47. https://doi.org/ 10.1016/S0167-6105(99)00059-8

Hazra, A., Mukhopadhyay, P., Taraphdar, S., Chen, J.-P., & Cotton, W. R. (2013). Impact of aerosols on tropical cyclones: An investigation using convection-permitting model simulation. *Journal of Geophysical Research: Atmospheres*, *118*(13), 7157–7168. https://doi.org/10.1002/jgrd.50546

Herbener, S. R., van den Heever, S. C., Carrió, G. G., Saleeby, S. M., & Cotton, W. R. (2014). Aerosol indirect effects on idealized tropical cyclone dynamics. *Journal of the Atmospheric Sciences*, *71*(6), 2040–2055. https://doi.org/10.1175/JAS-D-13-0202.1

Hersbach, H., Bell, B., Berrisford, P., Hirahara, S., Horányi, A., Muñoz-Sabater, J., Nicolas, J., Peubey, C., Radu, R., Schepers, D., Simmons, A., Soci, C., Abdalla, S., Abellan, X., Balsamo, G., Bechtold, P., Biavati, G., Bidlot, J., Bonavita, M., ... Thépaut, J.-N. (2020). The ERA5 global reanalysis. *Quarterly Journal of the Royal Meteorological Society*, *146*(730), 1999–2049. https://doi.org/10.1002/qj. 3803

Hogan, R. J., & Bozzo, A. (2016). *ECRAD: A new radiation scheme for the IFS*. European Centre for Medium-Range Weather Forecasts.

Hogan, R. J., & Bozzo, A. (2018). A flexible and efficient radiation scheme for the ECMWF model. *Journal of Advances in Modeling Earth Systems*, *10*(8), 1990–2008. https://doi.org/10.1029/2018MS001364

6. References

Holland, G. J. (1983). Angular momentum transports in tropical cyclones. *Quarterly Journal of the Royal Meteorological Society*, *109*(459), 187–209. https://doi.org/10.1002/qj.49710945909

Holton, J. R., & Hakim, G. J. (2013). *An introduction to dynamic meteorology* (J. R. Holton & G. J. Hakim, Eds.; Fifth Edition). Academic Press. https://doi.org/10.1016/C2009-0-63394-8

Huffman, G. J., Adler, R. F., Bolvin, D. T., & Nelkin, E. J. (2010). The TRMM multi-satellite precipitation analysis (TMPA). In M. Gebremichael & F. Hossain (Eds.), *Satellite rainfall applications for surface hydrology* (pp. 3–22). Springer Netherlands. https://doi.org/10.1007/978-90-481-2915-7_1

Jiang, B., Huang, B., Lin, W., & Xu, S. (2016). Investigation of the effects of anthropogenic pollution on typhoon precipitation and microphysical processes using WRF-Chem. *Journal of the Atmospheric Sciences*, *73*(4), 1593–1610. https://doi.org/10.1175/JAS-D-15-0202.1

Khain, A., Lynn, B., & Dudhia, J. (2010). Aerosol effects on intensity of landfalling hurricanes as seen from simulations with the WRF model with spectral bin microphysics. *Journal of the Atmospheric Sciences*, *67*(2), 365–384. https://doi.org/10.1175/2009JAS3210.1

Khain, A., Cohen, N., Lynn, B., & Pokrovsky, A. (2008). Possible aerosol effects on lightning activity and structure of hurricanes. *Journal of the Atmospheric Sciences*, *65*(12), 3652–3677. https://doi.org/10.1175/2008JAS2678.1

Khain, A., Pokrovsky, A., Pinsky, M., Seifert, A., & Phillips, V. (2004). Simulation of effects of atmospheric aerosols on deep turbulent convective clouds using a spectral microphysics mixed-phase cumulus cloud model. part I: Model description and possible applications. *Journal of the Atmospheric Sciences*, *61*(24), 2963–2982. https://doi.org/10.1175/JAS-3350.1

Khain, A., Rosenfeld, D., & Pokrovsky, A. (2005). Aerosol impact on the dynamics and microphysics of deep convective clouds. *Quarterly Journal of the Royal Meteorological Society*, *131*(611), 2639–2663. https://doi.org/10.1256/qj.04.62

6. References

Khain, A., & Sednev, I. (1996). Simulation of precipitation formation in the eastern mediterranean coastal zone using a spectral microphysics cloud ensemble model. *Atmospheric Research*, *43*(1), 77–110. https://doi.org/10.1016/S0169-8095(96)00005-1

Kleppek, S., Muccione, V., Raible, C. C., Bresch, D. N., Koellner-Heck, P., & Stocker, T. F. (2008). Tropical cyclones in ERA-40: A detection and tracking method. *Geophysical Research Letters*, *35*(10). https://doi.org/10.1029/2008GL033880

Lamb, D., & Verlinde, J. (2011). *Physics and chemistry of clouds*. Cambridge University Press. https://doi.org/10.1017/CBO9780511976377

Levy, R. C., Mattoo, S., Munchak, L. A., Remer, L. A., Sayer, A. M., Patadia, F., & Hsu, N. C. (2013). The collection 6 MODIS aerosol products over land and ocean. *Atmospheric Measurement Techniques*, *6*(11), 2989–3034. https://doi.org/10.5194/amt-6-2989-2013

Liang, Z., Ding, J., Fei, J., Cheng, X., & Huang, X. (2021). Direct/indirect effects of aerosols and their separate contributions to typhoon Lupit (2009): Eyewall versus peripheral rainbands. *Science China Earth Sciences*, *64*(12), 2113–2128. https://doi.org/10.1007/s11430-020-9816-7

Lin, W., Xu, S., & Sui, C.-H. (2011). A numerical simulation of the effect of the number concentration of cloud droplets on typhoon Chanchu. *Meteorology and Atmospheric Physics*, *113*(3), 99–108. https://doi.org/10.1007/s00703-011-0152-x

Lin, Y., Zhao, M., & Zhang, M. (2015). Tropical cyclone rainfall area controlled by relative sea surface temperature. *Nature Communications*, *6*(1), 1–7. https://doi.org/10.1038/ncomms7591

Lohmann, U., & Feichter, J. (2005). Global indirect aerosol effects: A review. *Atmospheric Chemistry and Physics*, *5*(3), 715–737. https://doi.org/10.5194/acp-5-715-2005

Lohmann, U., Lüönd, F., & Mahrt, F. (2016). *An introduction to clouds: From the microscale to climate*. Cambridge University Press. https://doi.org/10.1017/CBO9781139087513

6. References

Ma, P.-L., Zhang, K., Shi, J. J., Matsui, T., & Arking, A. (2012). Direct radiative effect of mineral dust on the development of African easterly waves in late summer, 2003–07. *Journal of Applied Meteorology and Climatology*, *51*(12), 2090–2104. https://doi.org/10.1175/JAMC-D-11-0215.1

Michalakes, J., Chen, S., Dudhia, J., Hart, L., Klemp, J., Middlecoff, J., & Skamarock, W. (2001). Development of a next-generation regional weather research and forecast model. In *Developments in teracomputing* (pp. 269–276). https://doi.org/10.1142/9789812799685_0024

Michalakes, J., Dudhia, J., Gill, D., Henderson, T., Klemp, J., Skamarock, W., & Wang, W. (2005). The weather research and forecast model: Software architecture and performance. In *Use of high performance computing in meteorology* (pp. 156–168). https://doi.org/10.1142/9789812701831_0012

Montgomery, M. T., & Smith, R. K. (2014). Paradigms for tropical cyclone intensification. *Australian Meteorological and Oceanographic Journal*, *64*(1), 37–66.

Montgomery, M. T., & Smith, R. K. (2017). Recent developments in the fluid dynamics of tropical cyclones. *Annual Review of Fluid Mechanics*, *49*(1), 541–574. https://doi.org/10.1146/annurev-fluid-010816-060022

Needham, H. F., Keim, B. D., & Sathiaraj, D. (2015). A review of tropical cyclone-generated storm surges: Global data sources, observations, and impacts. *Reviews of Geophysics*, *53*(2), 545–591. https://doi.org/10.1002/2014RG000477

NOAA Hurricane Research Division. (2017). 70th anniversary of the first hurricane seeding experiment [Accessed: 2022-05-07].

Norcross, B. (2007). *Hurricane almanac: The essential guide to storms past, present, and future*. St. Martin's Griffin.

Nordhaus, W. D. (2006). The economics of hurricanes in the United States. https://doi.org/10.3386/w12813

Powell, M. D., & Reinhold, T. A. (2007). Tropical cyclone destructive potential by integrated kinetic energy. *Bulletin of the American Meteorological Society*, *88*(4), 513–526. https://doi.org/10.1175/BAMS-88-4-513

6. References

Rosenfeld, D., Khain, A., Lynn, B., & Woodley, W. L. (2007). Simulation of hurricane response to suppression of warm rain by sub-micron aerosols. *Atmospheric Chemistry and Physics*, *7*(13), 3411–3424. https://doi.org/10.5194/acp-7-3411-2007

Rosenfeld, D., Clavner, M., & Nirel, R. (2011). Pollution and dust aerosols modulating tropical cyclones intensities. *Atmospheric Research*, *102*(1), 66–76. https://doi.org/10.1016/j.atmosres.2011.06.006

Rosenfeld, D., Woodley, W. L., Khain, A., Cotton, W. R., Carrió, G., Ginis, I., & Golden, J. H. (2012). Aerosol effects on microstructure and intensity of tropical cyclones. *Bulletin of the American Meteorological Society*, *93*(7), 987–1001. https://doi.org/10.1175/BAMS-D-11-00147.1

Segal, Y., & Khain, A. (2006). Dependence of droplet concentration on aerosol conditions in different cloud types: Application to droplet concentration parameterization of aerosol conditions. *Journal of Geophysical Research: Atmospheres*, *111*(D15). https://doi.org/10.1029/2005JD006561

Seifert, A., & Beheng, K. D. (2006). A two-moment cloud microphysics parameterization for mixed-phase clouds. part 1: Model description. *Meteorology and Atmospheric Physics*, *92*(1), 45–66. https://doi.org/10.1007/s00703-005-0112-4

Sitkowski, M., Kossin, J. P., & Rozoff, C. M. (2011). Intensity and structure changes during hurricane eyewall replacement cycles. *Monthly Weather Review*, *139*(12), 3829–3847. https://doi.org/10.1175/MWR-D-11-00034.1

Skamarock, W. C., Klemp, J. B., Dudhia, J., Gill, D. O., Barker, D. M., Wang, W., & Powers, J. G. (2005). *A description of the advanced research WRF version 2* (tech. rep.). National Center For Atmospheric Research Boulder Co Mesoscale and Microscale . . .

Smith, R. K. (1981). The cyclostrophic adjustment of vortices with application to tropical cyclone modification. *Journal of Atmospheric Sciences*, *38*(9), 2021–2030. https://doi.org/10.1175/1520-0469(1981)038<2021:TCAOVW>2.0.CO;2

6. References

Smith, R. K., Montgomery, M. T., & Van Sang, N. (2009). Tropical cyclone spin-up revisited. *Quarterly Journal of the Royal Meteorological Society*, *135*(642), 1321–1335. https://doi.org/10.1002/qj.428

Wang, Y.-q., & Wu, C.-C. (2004). Current understanding of tropical cyclone structure and intensity changes–a review. *Meteorology and Atmospheric Physics*, *87*(4), 257–278. https://doi.org/10.1007/s00703-003-0055-6

Willoughby, H. E., Clos, J. A., & Shoreibah, M. G. (1982). Concentric eye walls, secondary wind maxima, and the evolution of the hurricane vortex. *Journal of Atmospheric Sciences*, *39*(2), 395–411. https://doi.org/10.1175/1520-0469(1982) 039<0395:CEWSWM>2.0.CO;2

Willoughby, H. E., Jorgensen, D. P., Black, R. A., & Rosenthal, S. L. (1985). Project STORMFURY: A scientific chronicle 1962–1983. *Bulletin of the American Meteorological Society*, *66*(5), 505–514. https://doi.org/10.1175/1520-0477(1985) 066<0505:PSASC>2.0.CO;2

Woodruff, J. D., Irish, J. L., & Camargo, S. J. (2013). Coastal flooding by tropical cyclones and sea-level rise. *Nature*, *504*(7478), 44–52. https://doi.org/10.1038/nature12855

Wu, L. (2007). Impact of Saharan air layer on hurricane peak intensity. *Geophysical Research Letters*, *34*(9). https://doi.org/10.1029/2007GL029564

Zängl, G., Reinert, D., Rípodas, P., & Baldauf, M. (2015). The ICON (ICOsahedral Non-hydrostatic) modelling framework of DWD and MPI-M: Description of the non-hydrostatic dynamical core. *Quarterly Journal of the Royal Meteorological Society*, *141*(687), 563–579. https://doi.org/10.1002/qj.2378

Zhang, H., McFarquhar, G. M., Cotton, W. R., & Deng, Y. (2009). Direct and indirect impacts of Saharan dust acting as cloud condensation nuclei on tropical cyclone eyewall development. *Geophysical Research Letters*, *36*(6). https://doi.org/10.1029/2009GL037276

6. References

Zhang, H., McFarquhar, G. M., Saleeby, S. M., & Cotton, W. R. (2007). Impacts of Saharan dust as CCN on the evolution of an idealized tropical cyclone. *Geophysical Research Letters*, *34*(14). https://doi.org/10.1029/2007GL029876

Zhao, C., Lin, Y., Wu, F., Wang, Y., Li, Z., Rosenfeld, D., & Wang, Y. (2018). Enlarging rainfall area of tropical cyclones by atmospheric aerosols. *Geophysical Research Letters*, *45*(16), 8604–8611. https://doi.org/10.1029/2018GL079427

Zhou, X., & Wang, B. (2011). Mechanism of concentric eyewall replacement cycles and associated intensity change. *Journal of the Atmospheric Sciences*, *68*(5), 972–988. https://doi.org/10.1175/2011JAS3575.1

A. Appendix

A.1. List of Acronyms

CCN Cloud condensation nuclei

CDNC Cloud droplet number concentration

ECMWF European Centre for Medium-Range Weather Forecasts

ERA5 ECMWF Reanalysis v5

ICON Icosahedral non-hydrostatic

INP Ice nucleating particles

MODIS Moderate Resolution Imaging Spectroradiometer

PGF Pressure gradient force

RAMS Regional Atmospheric Modeling System

SAL Saharan Air Layer

TC Tropical cyclone

WRF Weather Research & Forecasting

A.2. Tables

Table A.2.1.: Nominal heights of coordinate half levels (m). The full level is defined in the middle between the half levels (Giorgetta et al., 2018).

Half level	Nominal height of coordinate half levels (m)
0.5	23000
1.5	19611
2.5	17836
3.5	16438
4.5	15255
5.5	14217
6.5	13289
7.5	12445
8.5	11671
9.5	10956
10.5	10291
11.5	9670
12.5	9088
13.5	8540
14.5	8024
15.5	7536
16.5	7073
17.5	6635
18.5	6219
19.5	5823
20.5	5446
21.5	5088
22.5	4746
23.5	4421

24.5	4111
25.5	3815
26.5	3532
27.5	3263
28.5	3007
29.5	2762
30.5	2530
31.5	2308
32.5	2098
33.5	1898
34.5	1708
35.5	1528
36.5	1358
37.5	1198
38.5	1047
39.5	905
40.5	773
41.5	650
42.5	536
43.5	432
44.5	337
45.5	251
46.5	176
47.5	112
48.5	59
49.5	20
50.5	0

A.3. Figures
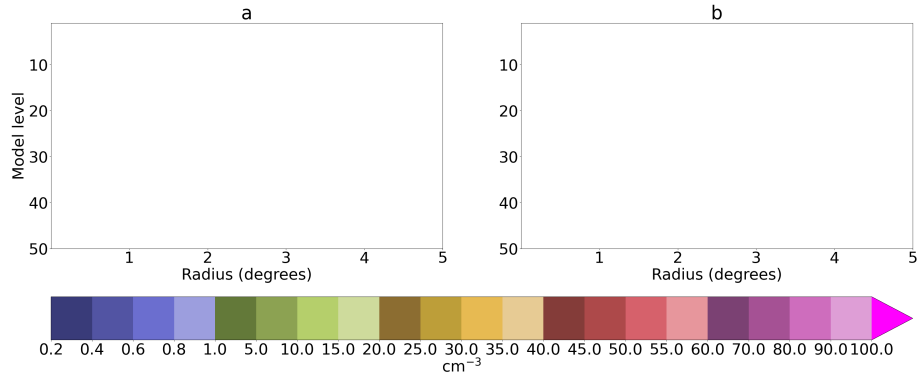
Figure A.1.: Azimuthal average of CDNC in the CTRL simulation of (a) TC1 and (b) TC2 at their respective T_{seed}.
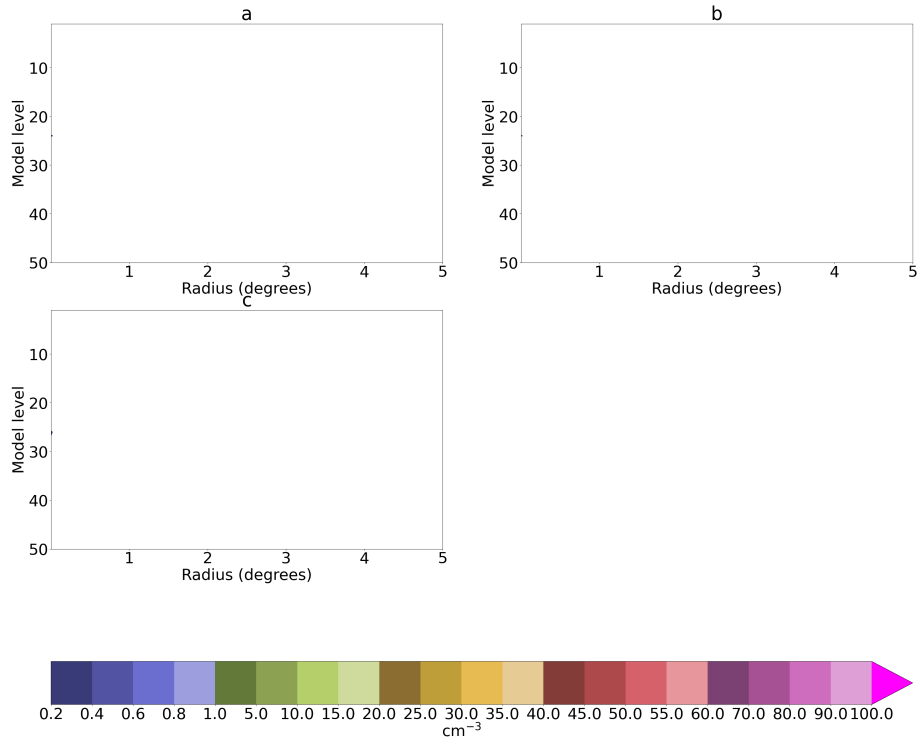
Figure A.2.: Azimuthal average of CDNC in (a) the L35E simulation at $T_{seed}+006h$, (b) the L29E simulation at $T_{seed}+006h$ and (c) the L29E simulation at $T_{seed}+012h$.
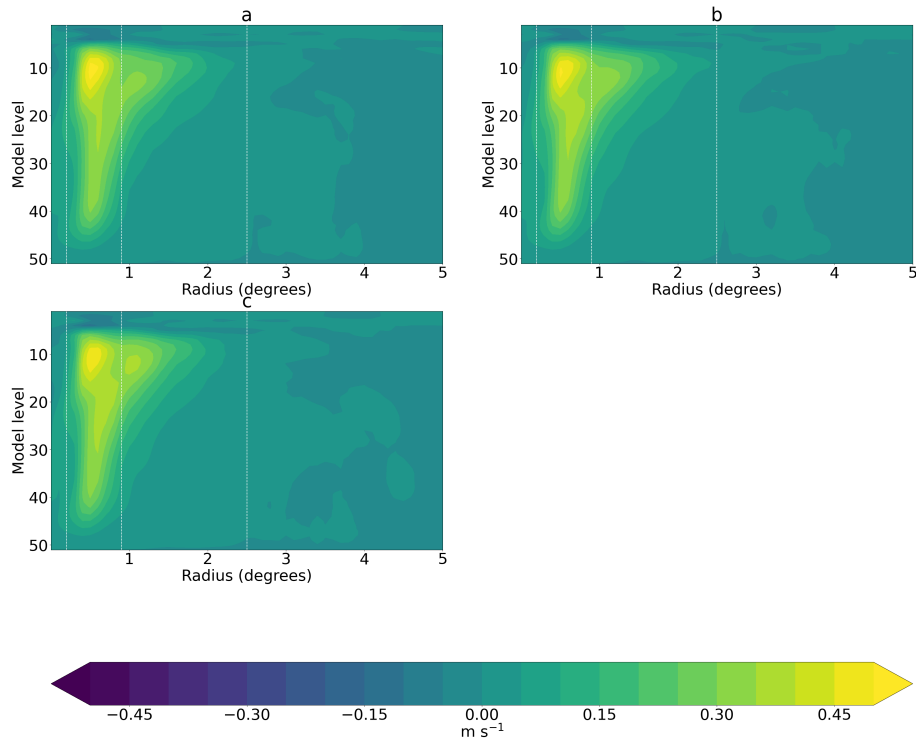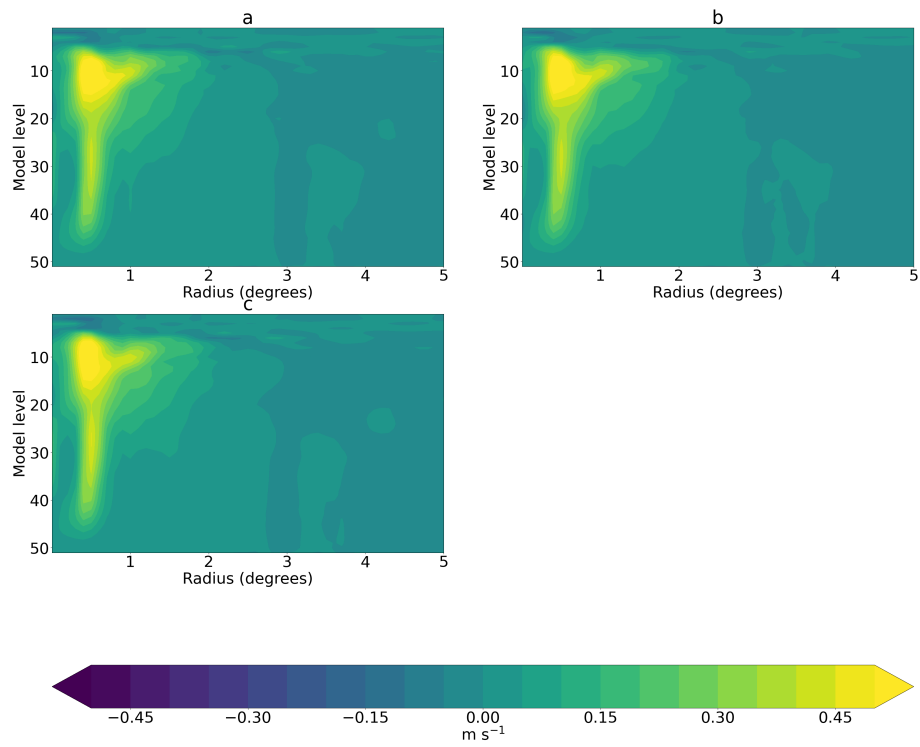
Figure A.3.: Azimuthal average of vertical velocity in (a) the L35E simulation, (b) the L29E simulation and (c) the L46W simulation, averaged between T_{seed} and time of landfall. White vertical dashed lines mark the defined eye, eyewall and far-field regions in the Hovmöller analyses.
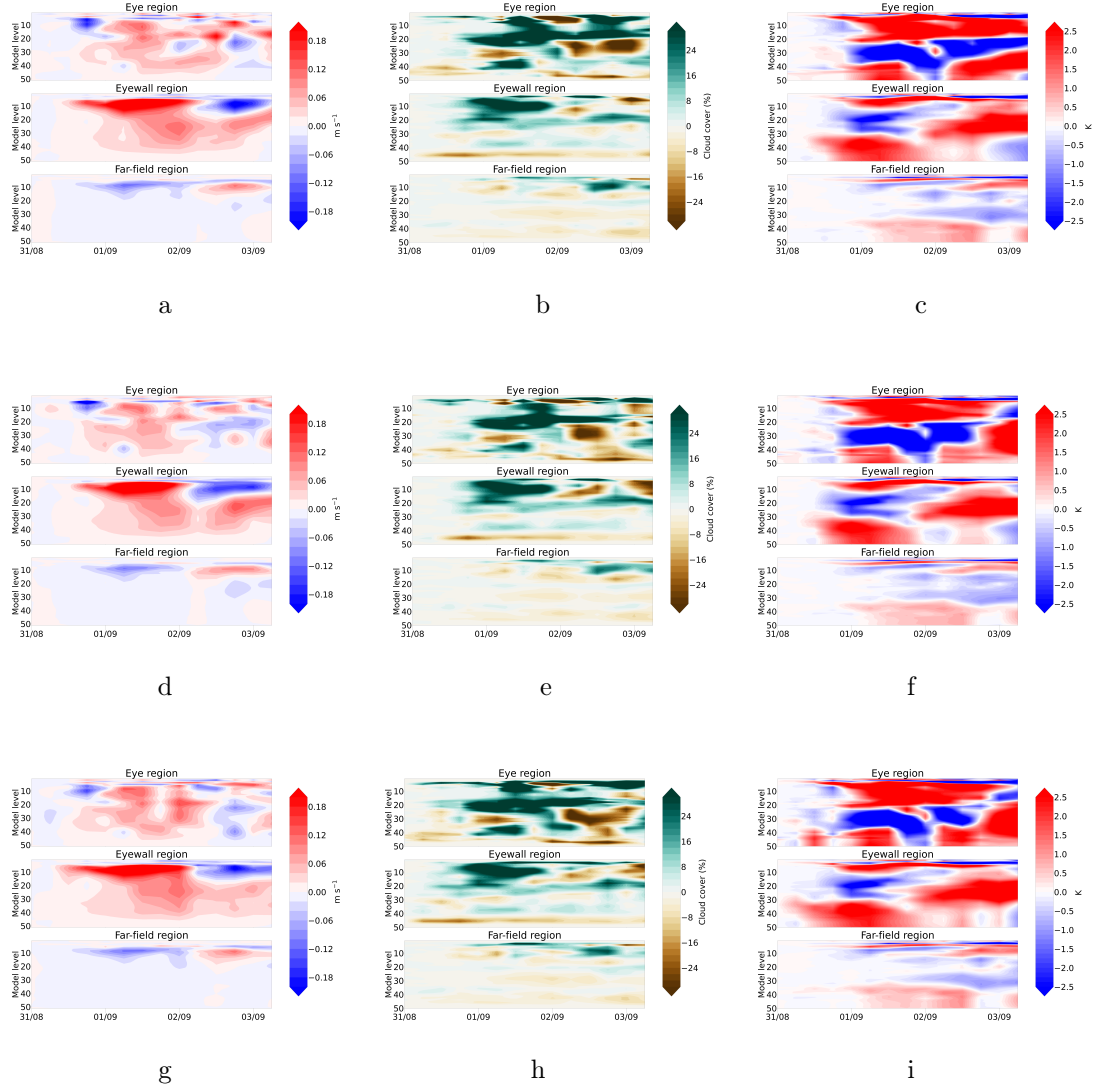
Figure A.4.: Hovmöller diagram of vertical velocity difference in (a) the L35E simulation, (d) the L29E simulation, (g) the L46W simulation, cloud cover difference in (b) the L35E simulation, (e) the L29E simulation, (h) the L46W simulation, θ_e difference in (c) the L35E simulation, (f) the L29E simulation and (i) the L46W simulation.
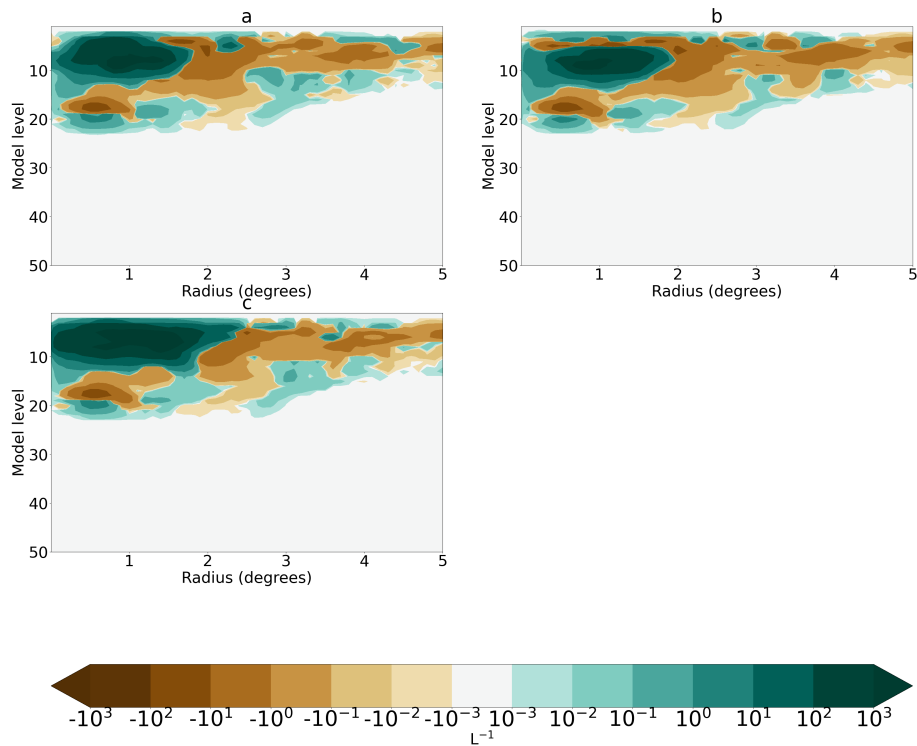
Figure A.5.: Azimuthal average of ice crystal number concentration difference in (a) the L35E simulation, (b) the L29E simulation and (c) the L46W simulation at $T_{seed}+036h$. Note that log scale is used in the plot.

Figure A.6.: Azimuthal average of vertical velocity in (a) the L35E simulation, (b) the L29E simulation and (c) the L46W simulation at $T_{seed}+036h$.

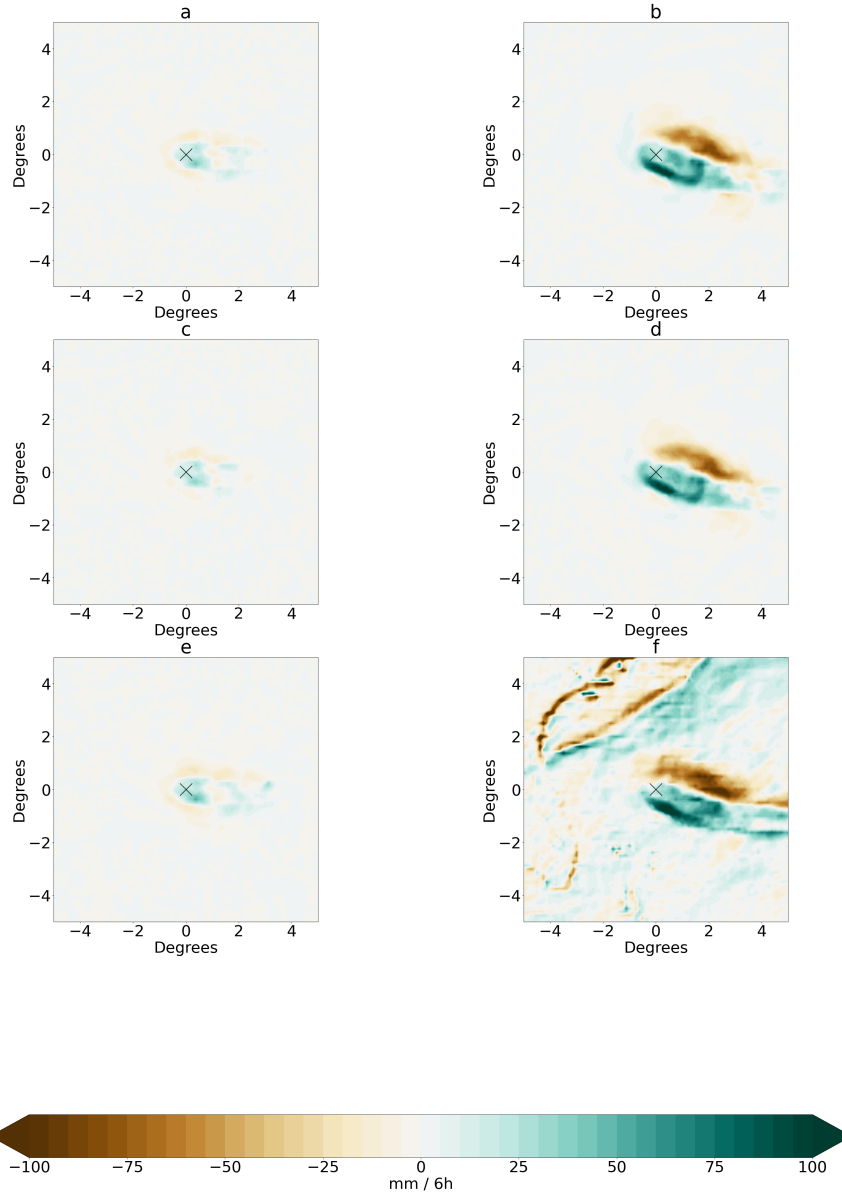Figure A.7.: Total precipitation difference in the L35E simulation at (a) T_{seed}+030h, (b) T_{seed}+054h, the L29E simulation at (c) T_{seed}+030h, (d) T_{seed}+054h, the L46W simulation at (e) T_{seed}+030h and (f) T_{seed}+054h. The black cross marks the origin and shows the centre of TC1. Difference was calculated by overlapping the TC centres in the respective simulations. Note that in (f) the centres of control TC and the perturbed TC were not at the same grid point, displaced by 0.125° in latitude and longitude respectively, such that the background is noisy.
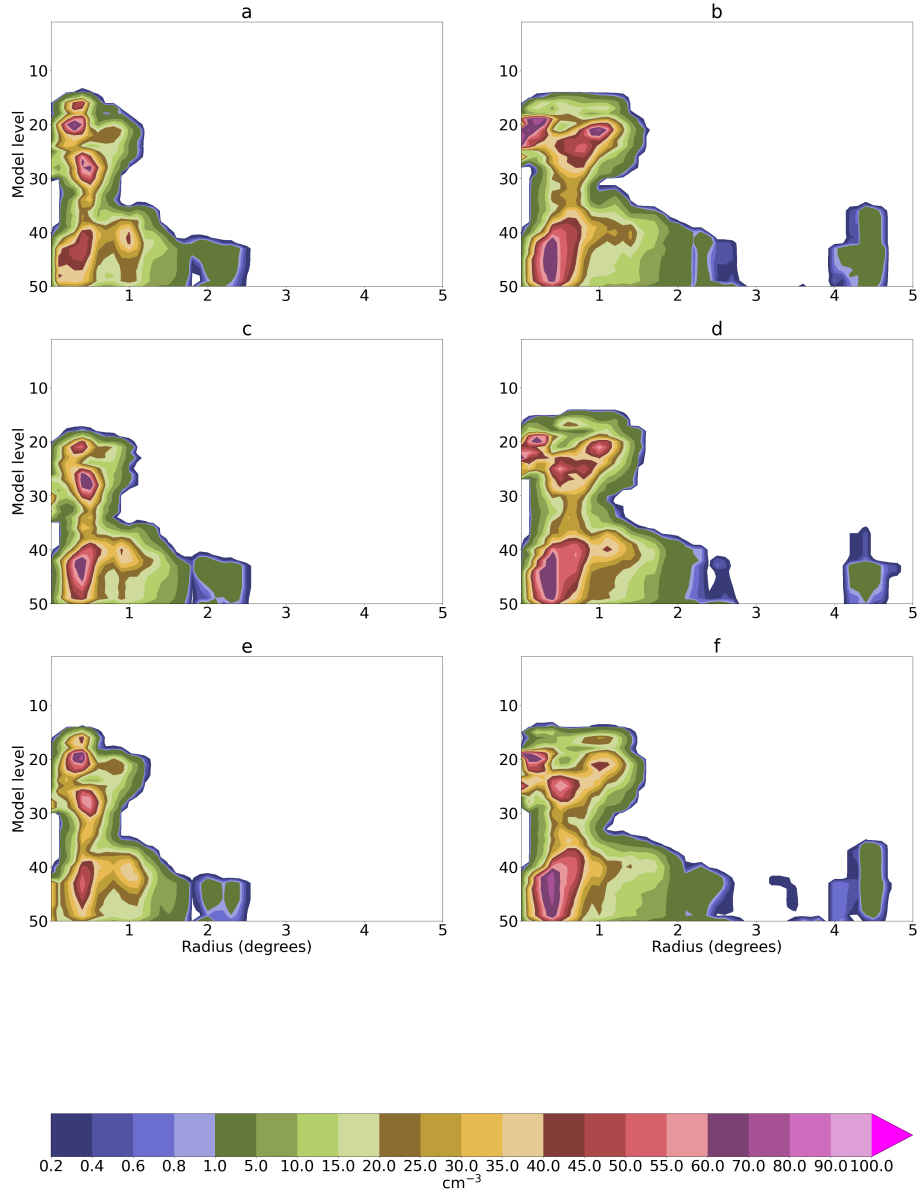
Figure A.8.: Azimuthal average of CDNC in the L35E simulation at (a) $T_{seed}+024h$, (b) $T_{seed}+048h$, the L29E simulation at (c) $T_{seed}+024h$, (d) $T_{seed}+048h$, the L46W simulation at (e) $T_{seed}+024h$ and (f) $T_{seed}+048h$.
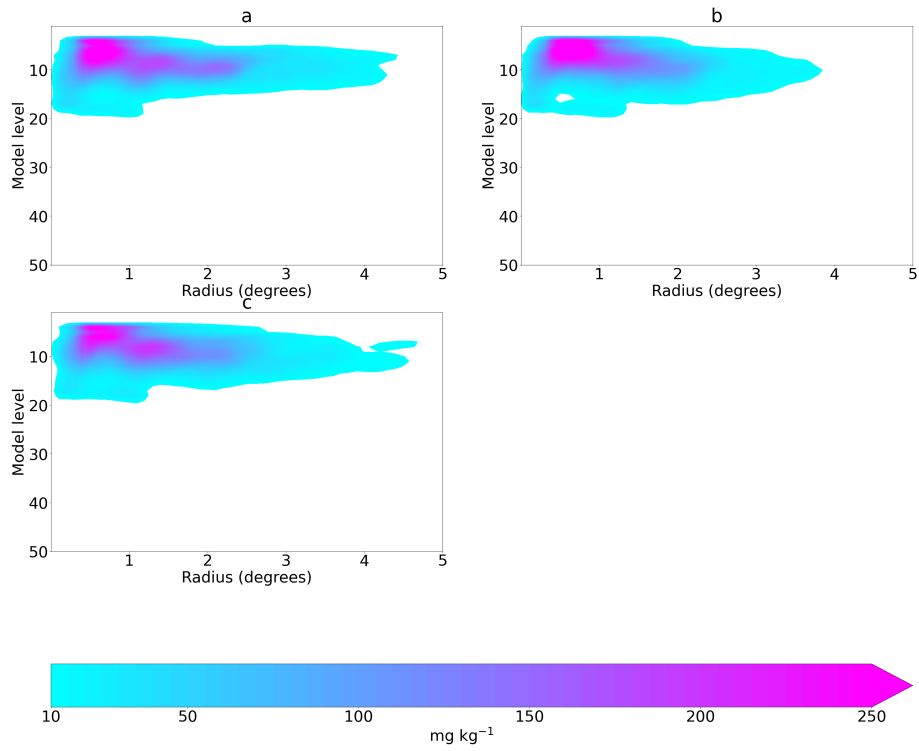
Figure A.9.: Azimuthal average of specific cloud ice content in (a) the L35E simulation, (b) the L29E simulation and (c) the L46W simulation at $T_{seed}+048h$.